European Journal of Medicinal Chemistry 220 (2021) 113475

Contents lists available at ScienceDirect

European Journal of Medicinal Chemistry

journal homepage: http://www.elsevier.com/locate/ejmech

Research paper

Beyond direct Nrf2 activation; reinvestigating 1,2,4-oxadiazole scaffold as a master key unlocking the antioxidant cellular machinery for cancer therapy

Mohammed Salah Ayoup [a, *], Marwa M. Abu-Serie [b], Hamida Abdel-Hamid [a], Mohamed Teleb [c, **]

[a] Chemistry Department, Faculty of Science, Alexandria University, Alexandria, 21321, Egypt
[b] Medical Biotechnology Department, Genetic Engineering and Biotechnology Research Institute, City of Scientific Research and Technological Applications, SRTA-City, Egypt
[c] Department of Pharmaceutical Chemistry, Faculty of Pharmacy, Alexandria University, Alexandria, 21521, Egypt

ARTICLE INFO

Article history:
Received 28 November 2020
Received in revised form
26 March 2021
Accepted 11 April 2021
Available online 16 April 2021

Keywords:
Antioxidant
Anticancer
1,2,4-Oxadiazole
Nrf2
TrxR
IKK
NF-kB
NADPH oxidase

ABSTRACT

Harnessing the antioxidant cellular machinery has sparked considerable interest as an efficient anticancer strategy. Activating Nrf2, the master switch of the cellular redox system, suppresses ROS, alleviates oxidative stress, and halts cancer progression. 1,2,4-oxadiazoles are iconic direct Nrf2 activators that disrupt Nrf2 interaction with its endogenous repressor Keap1. This study introduces rationally designed 1,2,4-oxadiazole derivatives that inhibit other Nrf2 suppressors (TrxR1, IKKα, and NF-kB) thus enhancing Nrf2 activation for preventing oxidative stress and carcinogenesis. Preliminary screening showed that the phenolic oxadiazoles **11, 15,** and **19** were comparable to ascorbic acid (ROS scavenging) and EDTA (iron chelation), and superior to doxorubicin against HepG-2, MDA-MB231, and Caco-2 cells. They suppressed ROS by 3 folds and activated Nrf2 by 2 folds in HepG-2 cells. Mechanistically, they inhibited TrxR1 (IC_{50}; 13.19, 17.89, and 9.21 nM) and IKKα (IC_{50}; 11.0, 15.94, and 19.58 nM), and downregulated NF-κB (7.6, 1.4 and 1.9 folds in HepG-2), respectively. They inhibited NADPH oxidase (IC_{50}; 16.4, 21.94, and 10.71 nM, respectively) that potentiates their antioxidant activities. Docking studies predicted their important structural features. Finally, they recorded drug-like *in silico* physicochemical properties, ADMET, and ligand efficiency metrics.

1. Introduction

Dysregulation of cellular energetics is a distinct hallmark in carcinogenesis [1]. As a consequence, cancer cells produce more reactive oxygen species (ROS) [2,3], which cause oxidative stress and promote various aspects of tumor progression ranging from evasion of apoptosis to tissue invasion, angiogenesis, and metastasis [4]. Hence, numerous anticancer agents were developed to prevent oxidative stress promoting carcinogenesis *via* scavenging ROS, inhibiting their production, and defending against their destructive attacks [5–9]. ROS levels were found tightly related to the nuclear factor erythroid 2 p45-related factor 2 (Nrf2) [3,4]; a cap'n'collar basic-leucine zipper transcription factor that ameliorates oxidative stress and restores redox homeostasis [10]. When activated in response to oxidative stress, Nrf2 transits to the nucleus and binds to Antioxidant/Electrophile Response Element (ARE/EpRE) in the promoter regions of the target genes. Its portfolio includes hundreds of genes expressing the key antioxidant enzymes and ROS scavengers; thioredoxin and glutathione systems [11,12]. It can also regulate cytosolic and mitochondrial ROS production by inhibiting NADPH oxidase (NOX) system [13,14]. Thus, Nrf2 is considered the master redox switch that turns on the cellular antioxidant signaling [15]. Accordingly, it has been validated as a druggable target for surmounting oxidative stress [16] and cancer chemoprevention [17]. This boosted research to introduce novel Nrf2 activators [18,19] and proceed to clinical trials [20]. Different chemical entities found their way as efficient Nrf2 activators [18,19,21] such as; fumaric acid esters [22], arylpyrazoles

* Corresponding author.
** Corresponding author.
E-mail addresses: mohammedsalahayoup@gmail.com, mohamed.salah@alexu.edu.eg (M.S. Ayoup), mohamed.t.ismail@alexu.edu.eg (M. Teleb).

https://doi.org/10.1016/j.ejmech.2021.113475
0223-5234/

[23,24], 1,4-diaminonaphthalene-based compounds [25], cyanoenone triterpenoids [26], and notably 1,2,4-oxadiazoles (Fig. 1) [18,27–31] that can also scavenge free radicals [32].

Nrf2 activation strategies rely on modulating its physiological regulation. Direct activators have been designed to disrupt the interaction between Nrf2 and its endogenous repressor Kelch-like ECH-associated protein 1 (Keap1) [33–36] However, additional Nrf2 regulation mechanisms do exist in parallel with or upstream of Keap1. Thioredoxin reductase 1 (TrxR1); the main thioredoxin system "engine" [37,38] operates in concert with Keap1 [34,35] and acts as a gatekeeper to guard against Nrf2 activation. Hence, direct TrxR1 inactivation, attenuation, or depletion promotes robust Nrf2 activation as supported by *Txnrd1* knockout or knockdown experiments [39–42]. Importantly, it was also observed that loss of TrxR1 activity can induce Nrf2 activation even in absence of general oxidative stress. Being a potent regulator of Nrf2, various TrxR inhibitors (Fig. 1) have been introduced as potential chemopreventive agents for cancer therapy [43–47].

Besides, another important crosstalk exists between Nrf2 and the transcription factor nuclear factor-κB (NF-κB) [48,49], where NF-κB directly inhibits Nrf2 at its transcriptional level. Also, the recruitment of histone deacetylase 3 by NF-κB causes local hypoacetylation that hinders Nrf2 signaling [50]. Further investigations revealed that the physical association of the NF-κB p65 subunit with Keap1 represses the Nrf2-ARE pathway [51] confirming that active NF-κB can suppress Nrf2 *via* multiple mechanisms. The classical and most known NF-κB pathway activation relies on activation of the IKK complex consisting of IKKα, IKKβ, and IKKγ [52]. In an alternative pathway, IKKα particularly plays a pivotal role [53]. Therefore, IKK may be considered as a key element in the interplay between Nrf2 and NF-κB, a regulator of Nrf2, and an important anticancer target as well [54].

2. Design strategy

Taken together, we set out our research protocol to synthesize a series of rationally designed 1,2,4-oxadiazole-based Nrf2 activators (Fig. 1) endowed with the potential to indirectly activate Nrf2 *via* suppressing Nrf2 negative regulators; TrxR, NF-κB, and IKK for enhancing Nrf2 activation and subsequent anticancer potential. In other words, the current study investigates expanding the antioxidant/anticancer potential of 1,2,4-oxadiazole scaffold beyond its

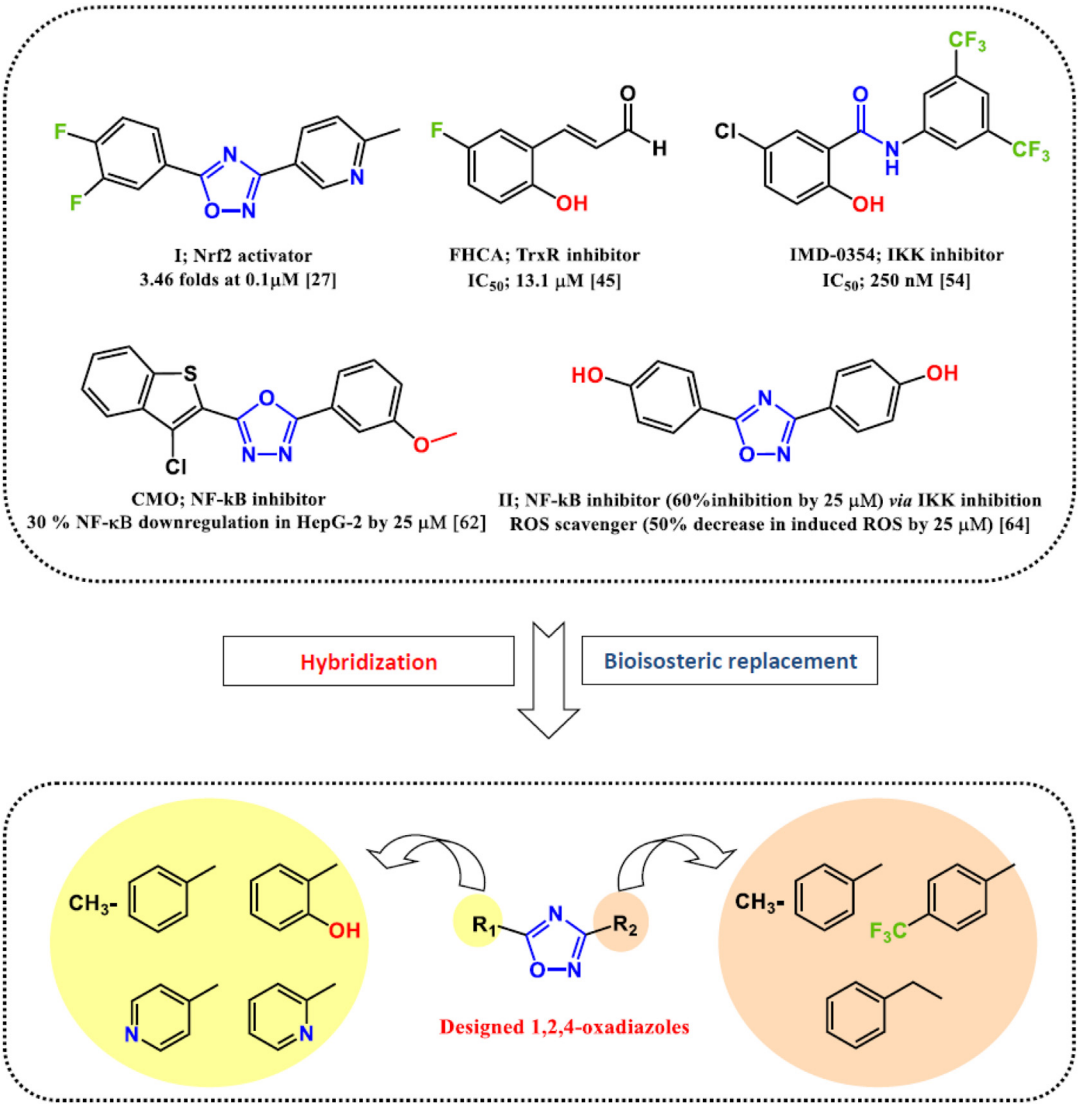

Fig. 1. Lead 1,2,4-oxadiazole-based Nrf2 activator [27], inhibitors of TrxR [45], IKK [54,64] and NF-κB [62,64], and ROS scavenger [64], and the designed multitarget 1,2,4-oxadiazole derivatives.

intrinsic direct Nrf2 activation. Accordingly, we started from the lead direct Nrf2 activator **I** [27] (Fig. 1) to tailor the target 1,2,4-oxadiazole-based "all in one" antioxidants for halting carcinogenesis based on the following considerations:

- Firstly; the chemical entity of 1,2,4-oxadiazole, being intrinsically π-electron deficient and may be susceptible to nucleophilic attack [55], sparked our interest to probe its activity against TrxR *via* possible interaction with the enzyme nucleophilic active site selenocysteine residue as common TrxR inhibitors do (e.g. FHCA, Fig. 1) [43–47,56].
- Secondly; the 1,2,4-oxadiazole core was rationalized as a non-classical isostere of the pharmacophoric amide moiety [57,58] in lead IKK inhibitors (e.g. IMD-0354, Fig. 1) that can also inhibit NF-κB [54,59–61].
- The 1,2,4-oxadiazole scaffold was also investigated for possible NF-κB targeting considering the structural resemblance with the reported 1,3,4-oxadiazole-based NF-κB inhibitors (e.g. CMO, Fig. 1), where the oxadiazole core contributes to the potency of NF-κB inhibition [58,62,63]. Furthermore, it was reported that 1,2,4-oxadiazole resveratrol analogs showed significant inhibitory activities against NF-kB and ROS production. The phenolic groups at 3 and 5 positions of the oxadiazole core (Compound II, Fig. 1) conferred prominent NF-kB activation to the oxadiazole core *via* inhibition of Ikk phosphorylation [64]. Another recent study showed that substituting the 1,2,4-oxadiazole scaffold with heterocyclic rings was also promising, where the 5-(furan-2-yl)-3-(1H-indol-5-yl)-1,2,4-oxadiazole exhibited potent NF-κB inhibition [65].
- Finally, the substitution pattern of the designed 1,2,4-oxadiazoles was directed to agree with the reported SAR studies on 1,2,4-oxadiazole-based Nrf2 activators [18,19], and to possibly mimic lead TxrR, IKK, and NF-κB inhibitors (Fig. 1). For instance, phenolic and fluorinated 1,2,4-oxadiazole derivatives were designed to possibly enhance the potency against TrxR based on the observation that hydroxylated and fluorinated TrxR inhibitors are more active than unsubstituted ones [45–47]. Interestingly, phenolic-substituted 1,2,4-oxadiazoles also possess intrinsic radical scavenging activities [32,64] that enhance their antioxidant potency.

All the target 1,2,4-oxadiazole derivatives (Fig. 1) were synthesized (Scheme 1) and preliminarily screened for their antioxidant and anticancer activities prior to mechanistic studies. In this regard, the compounds were evaluated for free radical scavenging activity and iron chelating efficiency that may be responsible for their antioxidant activities by reducing iron accumulation, thereby decreasing the hydroxyl radicals (ROS) generated by Fenton's reaction [66,67]. Besides, iron chelators are reported to inhibit NF-κB activation [68], hence affecting Nrf2 signaling. The compounds were then tested for their cytotoxic effect on normal fibroblasts (Wi-38) to assess their safety profiles, followed by evaluating their anticancer activities against three common human cancers, as indicated by the 2018 global cancer statistics [69,70], namely; liver (HepG-2), breast (MDA-MB231) and colon (Caco-2) *via* MTT assay [71–73]. Flow cytometric analysis was also performed to study their apoptotic induction potentials.

The most promising derivatives were evaluated for their potential to suppress intracellular ROS. Then, they were selected for further in-depth evaluation, where mechanistic studies were conducted to investigate their potential to inhibit Nrf2 negative regulators; TrxR, IKK, and NF-κB, and activate Nrf2. The compounds were also tested for their inhibitory activities against NADPH oxidase that reduces ROS. Docking simulations were conducted to predict their most probable binding modes and essential structural features contributing to interactions with the receptor sites. Also, their physicochemical parameters, pharmacokinetic profiles, and Ligand efficiency metrics namely; ligand efficiency (LE), lipophilic ligand efficiency (LLE), and ligand efficiency-dependent lipophilicity index (LELP) were also computed [74–80] for assessing and comparing the drug-likeness of the evaluated compounds.

3. Results and discussion

3.1. Chemistry

In this work, our strategy to synthesize a new series of 1,2,4-oxadiazole derivatives utilized an efficient economic method using DMSO/NaOH at ambient temperature under mild conditions with a simple workup protocol that can offer a broad range of alkyl or aryl derivatives [81]. The Amidoximes **2a-d** were prepared as previously described by refluxing the corresponding nitriles **1a-d** namely; benzonitrile, benzylnitrile, *p*-trifluoromethyl benzonitrile, and acetonitrile, respectively with hydroxylamine (50%) in ethanol [82–84] (Scheme 1). The crude amidoximes were purified by crystallization or by using silica gel. 3,5-Disubstituted 1,2,4-oxadiazoles **8**–**21** were then prepared easily by stirring the corresponding amidoximes **2a-d** with various carboxylic esters of benzoic, picolinic, isonicotinic, salicylic, or acetic acid **3**–**7** using the DMSO/NaOH protocol [81].

The structures of 3,5-disubstituted 1,2,4-oxadiazoles **8**–**21** were established based on their spectral data. ^{1}H NMR spectra of **8**–**21** showed aromatic protons signals at the range of δ_H: 8.89–7.01 ppm. The benzylic protons of **12**–**15** appeared at δ_H: 4.21–4.06 ppm. ^{1}H NMR of **20** and **21** showed the methyl protons as singlet signals at δ_H: 2.6 and 2.4 ppm, respectively. The phenolic protons of **11, 15,** and **19** appeared at δ_H: 10.57 and 10.7 ppm. ^{13}C NMR spectra of all the synthesized 1,2,4-oxadiazole derivatives showed the 1,2,4-oxadiazole ring carbons at values ranging from δ_C: 177.0 to 167.2 ppm. The phenolic ring carbons (C–OH) of **11**, **15**, and **19** were detected at δ_C: 157.2, 157.5, and 157.70 ppm, respectively. For all products, methyl carbons of **20** and **21** appeared at δ_C: 11.2 and 12.3 ppm, respectively. The ^{13}C NMR spectra of **16**–**20** showed characteristic signals corresponding to **C**F_3 at δ_C: 124.0–126.0 ppm. All the synthesized derivatives were also confirmed by mass spectroscopy. It is worth mentioning that the synthesis of 3-methyl-1,2,4-oxadiazole derivatives utilizing amidoxime **2d** with various esters did not proceed successfully under the NaOH/DMSO protocol.

3.2. Biological evaluation

3.2.1. Free radical scavenging and iron chelating activities

The antioxidant activities of all the synthesized 1,2,4-oxadiazoles were studied in terms of measuring their free radical scavenging and iron chelation potentials utilizing 1,1-Diphenyl-2-picrylhydrazyl (DPPH) assay [85] and 1,10-phenanthroline method [86], respectively. Results were reported as the inhibitory concentration at 50% DPPH radical scavenging (IC_{50}) and effective concentration of 50% iron chelation (EC_{50}) (Table 1). The free radical scavenging results showed that **11, 15,** and **19** exhibited the highest antioxidant activities with submicromolar IC_{50} (0.912, 0.585, and 0.423 μM, respectively), followed by **10**, **12**–**14, 18, 20,** and **21** (IC_{50} < 2 μM). Compounds **8**, **9,** and **17** were moderately active (IC_{50}; 2.176–3.442 μM), whereas **16** recorded the lowest activity. Interestingly, **15** and **19** were comparable to L-ascorbic acid. Regarding iron chelation, **11**, **15**, and **19** were the most potent derivatives (EC_{50}; 0.103, 0.045 and 0.063 μM, respectively). **10, 12**–**14, 18, 20** (EC_{50} < 0.2 μM) showed moderate activities, whereas the remaining compounds were less active (EC_{50}; 0.213–0.406 μM) (Table 1).

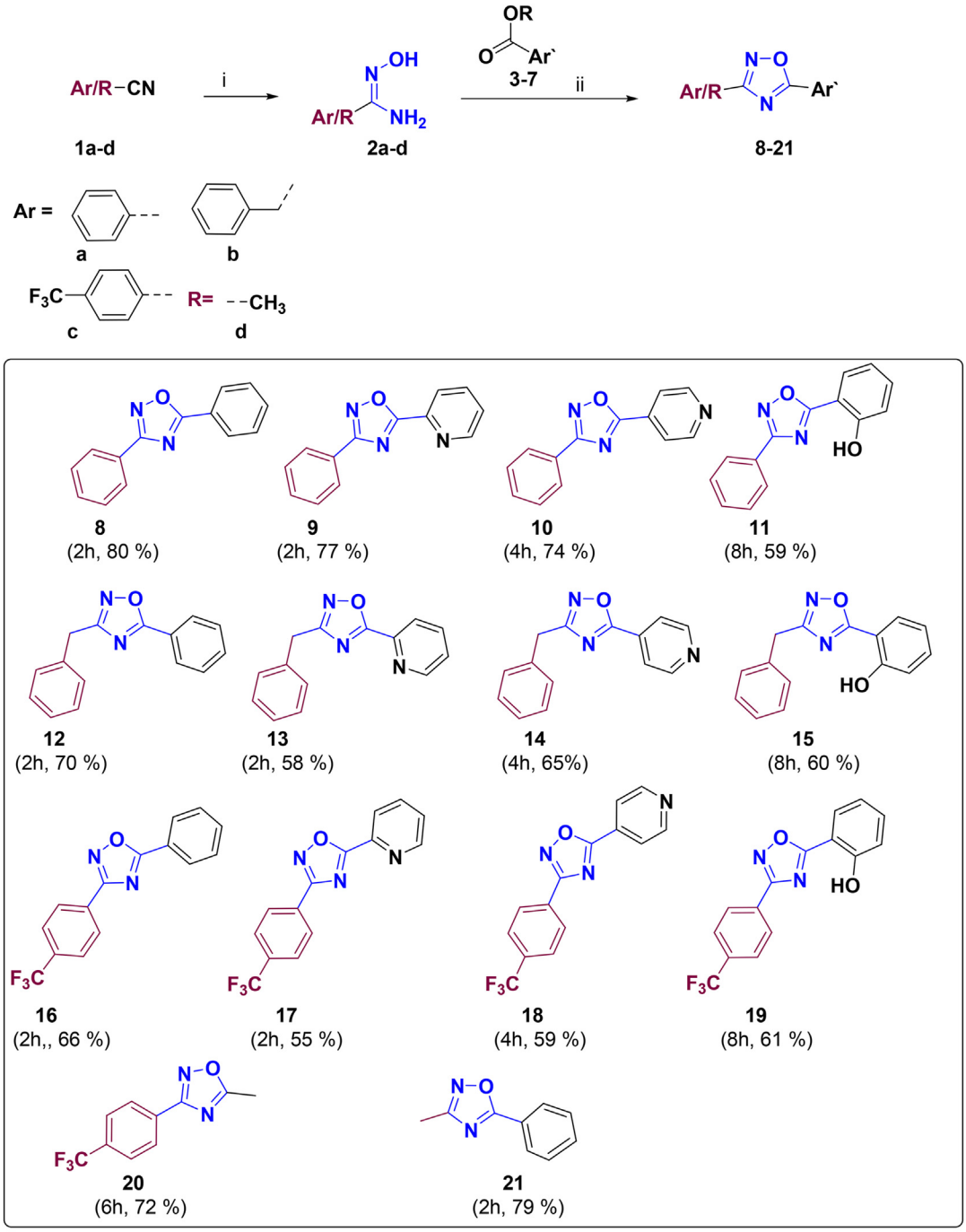

Reagents and conditions: (i) NH_2OH (50 %) / EtOH, Reflux, 4h; (ii) NaOH, DMSO, rt.

Scheme 1. Synthesis of 3,5-disubstituted 1,2,4-oxadiazoles **8**–**21.**

Again, **15** and **19** were as potent as the reference iron chelator EDTA. Since free radicals are the main initiators and promoters of carcinogenesis and metastasis [4], then the powerful antioxidant potential of **11**, **15**, and **19** represented by their efficient free radical scavenging and iron chelating activities may confer potential inhibition of tumor initiation and progression.

3.2.2. *Cytotoxicity screening and flow cytometric analysis*

All the synthesized oxadiazoles were screened for cytotoxic effects on normal human lung fibroblasts (Wi-38) to evaluate their safety profiles in terms of concentrations at 100% and 50% cell viability (EC_{100} and IC_{50}, respectively). Then, the compounds were evaluated for potential anticancer activities against three human cancers (HepG-2HepG-2, MDA-MB231, and Caco-2) compared to the reference chemotherapy; doxorubicin utilizing MTT assay (Table 2) [71–73] in an attempt to find a correlation between their anticancer and antioxidant activities (Table 1). Such correlation is usually highlighted in similar studies [87–90].

Interestingly, all the screened compounds were safer than doxorubicin (EC_{100}; 11.5 nM, IC_{50}; 34.1 nM) with **19** (EC_{100}; 72 nM,

Table 1
DPPH scavenging and iron chelating activities of the 3,5-disubstituted 1,2,4-oxadiazoles **8**–**21**.

Compound No.	IC_{50} (μM)	EC_{50} (μM)
8	3.041 ± 0.019	0.328 ± 0.023
9	2.176 ± 0.018	0.219 ± 0.019
10	1.973 ± 0.041	0.185 ± 0.005
11	**0.912 ± 0.005**	**0.103 ± 0.010**
12	1.343 ± 0.050	0.124 ± 0.004
13	1.164 ± 0.014	0.118 ± 0.010
14	1.288 ± 0.033	0.110 ± 0.005
15	**0.585 ± 0.009**	**0.045 ± 0.001**
16	5.625 ± 2.110	0.406 ± 0.017
17	3.442 ± 0.947	0.297 ± 0.004
18	1.693 ± 0.129	0.154 ± 0.003
19	**0.423 ± 0.017**	**0.063 ± 0.000**
20	1.896 ± 0.134	0.177 ± 0.002
21	1.966 ± 0.089	0.213 ± 0.008
L-ascorbic acid	0.461 ± 0.024	ND
Na_2 -EDTA	ND	0.055 ± 0.004

*All values are expressed as mean ± standard error of the mean (SEM). ND; not determined.

IC_{50}; 352.3 nM) at the top of the list followed by **11** and **15**. Obviously, the same compounds (**11**, **15**, and **19**) exhibited excellent anticancer activities against the investigated cancer cell lines. **19** recorded the highest anticancer potency among the group and was superior to doxorubicin against the three cancers followed by **11** and **15**, respectively. **11** and **15** showed higher potency than doxorubicin against MDA-MB231 and Caco-2 but were slightly less active against HepG-2 cells. Other oxadiazoles showed different activity profiles against the screened cell lines. Concerning HepG-2 cells, compounds other than **11**, **15**, and **19** were less potent than doxorubicin and showed moderate to low anticancer activities. On the other hand, the activity pattern against MDA-MB231 seems to be "all or none", where all compounds were more active than doxorubicin except **9**, **10**, and **16** which were inactive. Surprisingly, **10** was more potent than doxorubicin against Caco-2 cells, followed by **13, 12**, and **9**. The remainders were less active.

Besides, assessing the selectivity of compounds towards cancerous cells rather than normal ones is a key to real anticancer evaluation. Herein, the selectivity index (SI) values were calculated (Table 1) as the ratio of IC_{50} values against normal and tumor cells. SI $\geq$ 3 generally acknowledges acceptable selectivity to the studied compounds [91] All derivatives were more selective than doxorubicin to HepG-2 (except **16** and **20**), MDA-MB231 (except **9**, **10**, and **16**), and Caco-2 cells (except **14**, **16**–**18**, and **20**). The highest selectivity values were detected for **19, 11**, and **15** against HepG-2 cells, for **18, 8**, and **17** against MDA-MB231, and **19**, **10**, and **11** against Caco-2 cells, respectively. The most potent anticancer derivatives **11, 15**, and **19** exceeded the acceptable SI limit against the three cancer cell lines, except for **15** against MDA-MB231. Accordingly, the three compounds were selected for further mechanistic studies.

HepG-2, MDA-MB231, and Caco-2 cells were examined morphologically after treatment with **11**, **15**, and **19** (at their respective EC_{100}; Table 2) in comparison with doxorubicin-treated cells and the untreated ones (Fig. 2). As seen, the cancerous cells treated with 11, 15, and 19 lost their characteristic shape and suffered severe shrinkage due to the potent apoptotic potential of the evaluated compounds relative to the control [80,92]. It is noteworthy to refer to the healthy morphology of Wi-38 cells that were treated with EC_{100} concentrations of these tested compounds to assess the safety of the selected compounds.

The respective IC_{50} of 11, 15, and 19 (Table 2) were then tested for their apoptotic induction potentials by flow cytometric annexin V/propidium iodide analysis in HepG-2, MDA-MB231, and Caco-2 cells. As illustrated (Fig. 3), 11 and 19 induced apoptosis-dependent anticancer activity by more than 55% in HepG-2 and Caco-2 cells, whereas 15 induced apoptosis by 64.2 and 47.4% in HepG-2 and Caco-2, respectively. The lowest percentages of the apoptotic cell population (28–37.9%) were recorded in the treated MDA-MB231 cells. Interestingly, 11, 15, and 19 revealed significantly higher apoptosis percentages in all treated human cancer cell lines (HepG-2, Caco-2, and MDA-MB231) than doxorubicin (45.3, 19.9, and 31.7%, respectively).

3.2.3. *Intracellular ROS scavenging activity*

The correlation between the anticancer activities of the investigated oxadiazoles (**11**, **15**, and **19**) and their ROS scavenging potencies was studied *via* quantifying the intracellular ROS levels in HepG-2 cells treated with their respective IC_{50} doses (Table 2) relative to controls (Fig. 4). The assay relies on the ability of the tested compounds to prevent the intracellular ROS-mediated oxidation of the non-fluorescent dichlorodihydrofluorescin diacetate ($DCFH_2$-DA) to the highly fluorescent DCF. Consequently, efficient intracellular ROS suppression indicates that the compound under investigation was able to enter the cell and act as a strong antioxidant. As declared (Fig. 4), the three promising anticancer

Table 2
Cytotoxicity of the 3,5-disubstituted 1,2,4-oxadiazoles **8**–**21**.

Compound No.	Wi-38		HepG-2		MDA-MB231		Caco-2	
	EC_{100} (nM)[a]	IC_{50} (nM)	IC_{50} (nM)	SI	IC_{50} (nM)	SI	IC_{50} (nM)	SI
8	26.3 ± 3	116.9 ± 2	53.9 ± 2	2.1	13.5 ± 15	8.6	51.6 ± 0.4	2.3
9	28.2 ± 2	126.1 ± 1	50.7 ± 2	2.4	Nil	_	39.7 ± 0.4	3.2
10	52.8 ± 2	186.8 ± 2	55.4 ± 6	3.3	Nil	_	12.1 ± 1	15.4
11	**65.1 ± 4**	**235.7 ± 7**	**23.5 ± 3**	**10.0**	**64.3 ± 2**	**3.6**	**25.1 ± 5**	**9.4**
12	35.2 ± 2	166.4 ± 1	87.7 ± 7	1.9	23.5 ± 7	3.7	37.1 ± 0.7	4.5
13	35.1 ± 0.4	166.4 ± 1	42.2 ± 0.3	3.9	11.8 ± 2	3.6	34.3 ± 0.2	4.9
14	39.3 ± 0.5	174.2 ± 2	49.8 ± 5	3.5	17.0 ± 9	2.9	Nil	_
15	**45.4 ± 4**	**196.2 ± 1**	**27.3 ± 1**	**7.2**	**78.6 ± 7**	**2.5**	**27.2 ± 0.7**	**7.2**
16	25.5 ± 2	110.8 ± 2	97.7 ± 19	1.1	Nil	_	317.6 ± 7	0.3
17	19.0 ± 0.4	107.9 ± 2	38.8 ± 2	2.8	13.9 ± 9	7.8	Nil	_
18	33.7 ± 2	148.1 ± 2	35.7 ± 3	4.1	11.2 ± 6	13.2	242.6 ± 21	0.6
19	**72.0 ± 2**	**352.3 ± 2**	**14.9 ± 3**	**23.6**	**61.8 ± 0.3**	**5.7**	**13.9 ± 0.6**	**25.3**
20	13.8 ± 1	62.9 ± 5	46.6 ± 3	1.3	18.6 ± 1	3.4	Nil	_
21	33.7 ± 5	148.5 ± 2	80.4 ± 6	1.8	49.6 ± 3	3.0	77.5 ± 7	1.9
DOX.	11.5 ± 1	34.1 ± 1	22 ± 4	1.5	106 ± 9	0.3	48.1 ± 3	0.7

[a] All values are expressed as mean ± SEM.

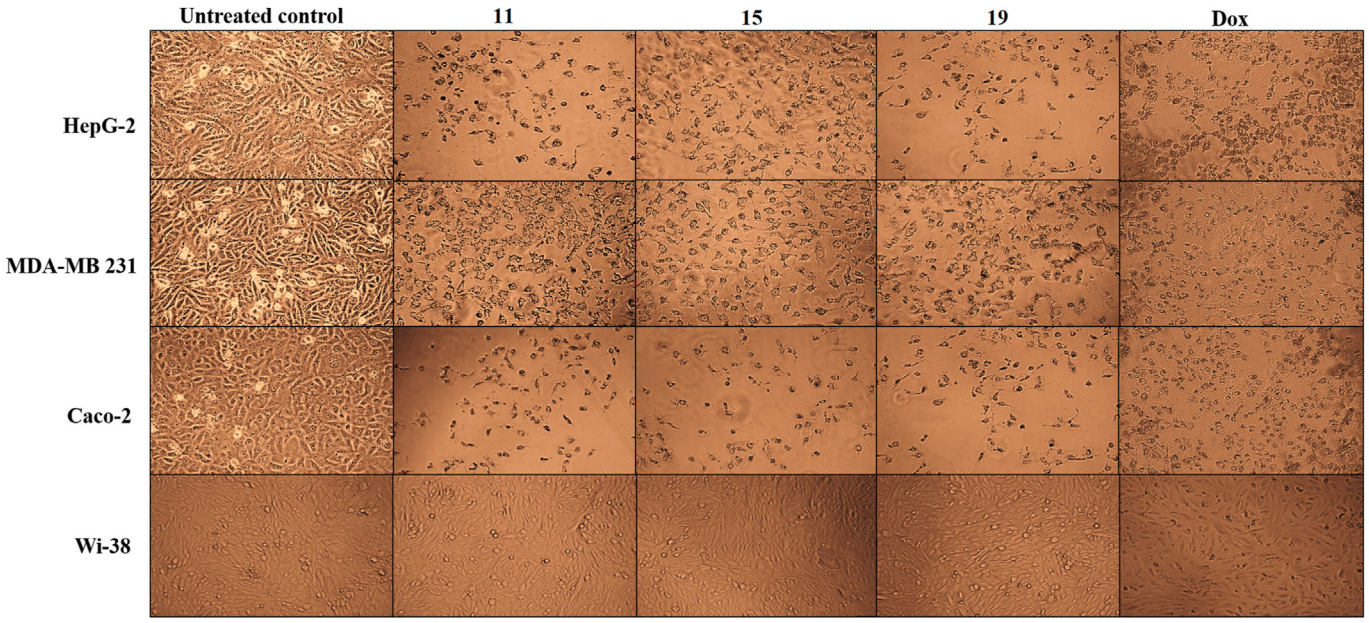

Fig. 2. Morphological alteration of the most active derivatives (11, 15, and 19)-treated HepG-2, MDA-MB231, Caco-2, and Wi-38 cells (at their relevant EC_{100} doses; Table 2) in comparison with doxorubicin-treated cells and the untreated control cells.

compounds were able to decrease ROS levels (i.e., the oxidized DCF) by about 3 folds compared to the untreated control HepG-2 cells. Their potencies were almost comparable (11.39 ± 1.15–11.99 ± 0.015%).

3.2.4. Nrf2 activation

A high throughput assay with a quick ELISA format was employed to evaluate the possible Nrf2 activation potential of the selected oxadiazoles (**11**, **15**, and **19**) at their respective safe (EC_{100}) doses (Table 2). As seen (Fig. 5), **11**, **15**, and **19** induced Nrf2 activity by 2.36, 1.78, and 2.04 folds, respectively in the treated HepG-2 cells relative to the untreated cells. It is worth mentioning that the Nrf2 induction activities of the most active derivatives **11** and **19** at their EC_{100} doses (65.1 and 72 nM, respectively) were comparable to that of the lead 1,2,4-oxadiazole-based Nrf2 activator **I** (Fig. 1) exhibiting 3.46 folds activation at 100 nM [27].

3.2.5. TrxR1 inhibition

In light of the previously mentioned results, *in vitro* TrxR1 inhibitory activities of the most promising oxadiazoles **11**, **15**, and **19** were also explored in comparison to staurosporine [93,94] utilizing the specific colorimetric assay kit. Results (Table 3) showed that they were more potent than the reference staurosporine as well as the lead cinnamaldehyde derivative **FHCA** [45] (Fig. 1). **19** was nearly 2-fold more potent than **15**, whereas **11** was relatively moderate. Ligand efficiency metrics were also computed as reported [74–80] for assessing and comparing the drug-likeness of the evaluated compounds. The three derivatives succeeded to pass the acceptable limits for LE (0.3) [74–76], score lead-like LLE (≥3) [76–78], and fall within the optimal LELP range −10<LELP<10 [76]. Obviously, **11** recorded the highest LE and LLE, whereas **19** scored the highest LELP value.

3.2.6. IKKα inhibition

In vitro IKKα inhibition profiles of the selected oxadiazoles (Table 4) were recorded employing a luminescent kinase assay. The evaluated derivatives were more active than the reference; staurosporine [95]. **19** was slightly more active than **11** and 1.5-fold more potent than **15.** Their ligand efficiency metrics were acceptable [74–80]. Again, **11** recorded the highest LE and LLE, whereas **19** scored the highest LELP.

3.2.7. Inhibition of NF-κB

Quantitative real-time PCR analysis revealed the NF-κB expression in HepG-2 cells incubated for 72 h with IC_{50} doses of the studied derivatives **11**, **15,** and **19** was reduced to 13.1, 68.85, and 51.95%, respectively. In other words, **11**, **15**, and **19** downregulated the expression level of NF-kB in the treated HepG-2 cells (at their respective IC_{50} doses) by 7.6, 1.4, and 1.9 folds, respectively, relative to the untreated cells (Fig. 6). In contrast, doxorubicin [96] increased the expression level of NF-kB by 1.72 folds in the treated HepG-2 cells relative to the untreated control cells. It is noted that 25 μM of the lead 1,3,4-oxadiazole-based NF-κB inhibitor **CMO** (Fig. 1) downregulated NF-kB in HepG-2 cells to approximately 70% after 12 h incubation [62]. Another study reported that the lead 1,2,4-oxadiazole derivative **II** (Fig. 1) suppressed NF-κB signaling *via* inhibiting IKKα phosphorylation at 25 μM [64].

3.2.8. NADPH oxidase inhibition

NADPH oxidase (NOX) inhibition profiles of the investigated compounds were detected by quantitative sandwich enzyme immunoassay technique utilizing the specific ELISA kit. Results (Table 5) showed that **19** was the most potent among the group [97], followed by **11.15** was the least active derivative. **19** was 2-fold more potent than **15**. Their ligand efficiency metrics were acceptable [74–80]. Again, **11** recorded the highest LE and LLE values, whereas **19** scored the highest LELP.

3.3. Structure-activity relationship

The preliminary antioxidant screening pattern revealed that the designed oxadiazole scaffolds (Fig. 1) conserved their intrinsic antioxidant activities. The antioxidant potency in terms of free radical scavenging and iron chelating activities was found to be a function of substitution pattern (Fig. 7). As expected, the phenolic derivatives **11**, **15**, and **19** exhibited the highest potential to suppress free radicals among the series. It is known that phenolic hydroxyl groups are good hydrogen donors that can react with ROS in

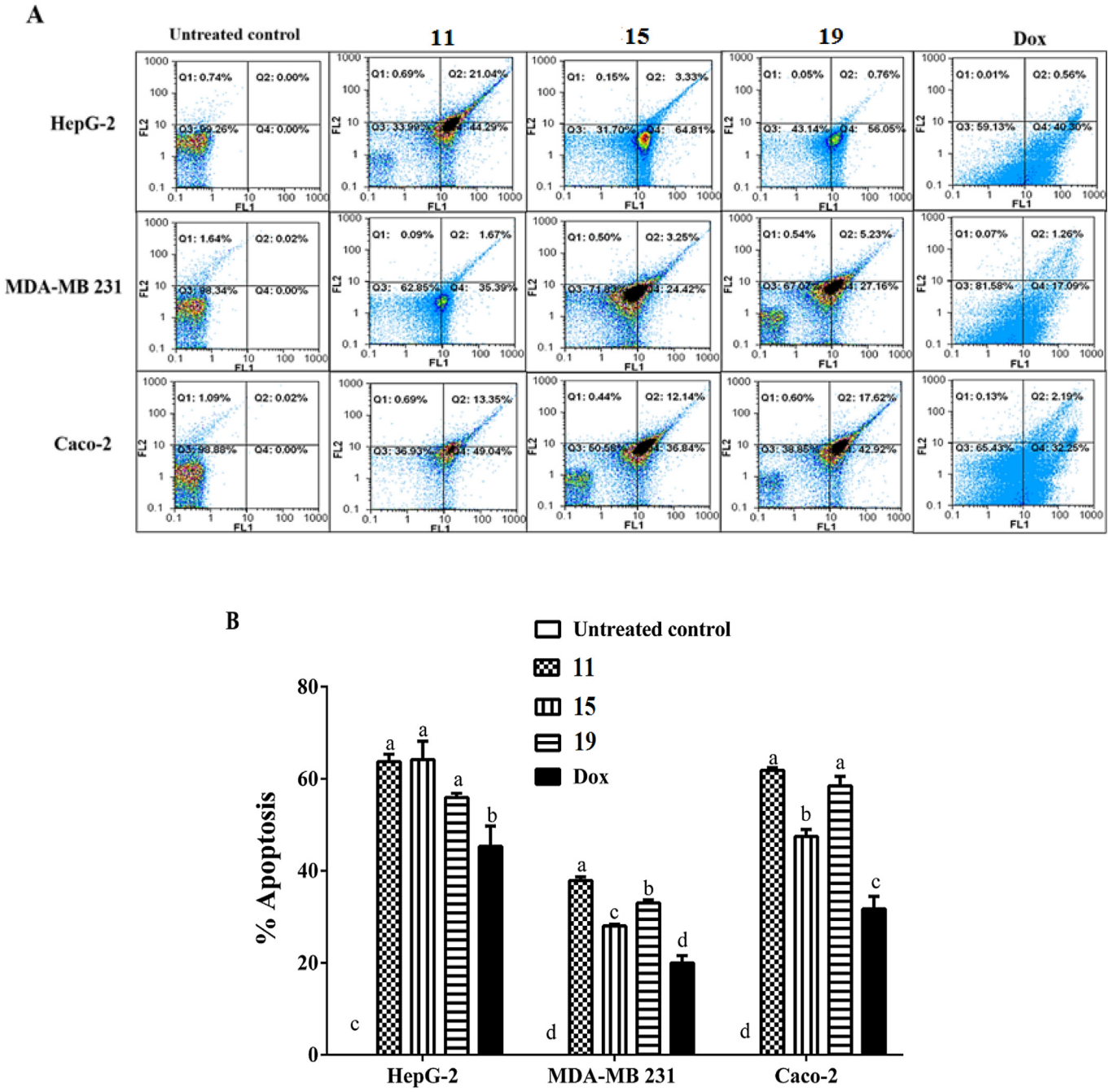

Fig. 3. **(A)** Flow charts of annexin-PI analysis of the HepG-2, MDA-MB231, and Caco-2 cells treated with the respective IC_{50} of **11**, **15**, and **19** (Table 2). **(B)** The relative apoptotic cell population percentages. All values are expressed as mean ± SEM. Different letters are significantly different at $P < 0.05$.

a termination reaction that breaks the cycle of new ROS generation. After interaction with ROS, a relatively long-lived radical form of the phenolic antioxidant compound that is much more stable than the initial ROS is produced. This stability is attributed to the interaction with the aromatic π-electrons [98]. Within the studied phenolic derivatives, the 3-trifluoromethylphenyl substituted oxadiazole **19** was the most potent free radical scavenger followed by the 3-benzyl derivative **15** and the 3-phenyl analog **11**, respectively. This may be due to the stabilizing effect of the trifluoromethyl electron-withdrawing behavior on the corresponding generated phenolic radical during participation in the antioxidant process. Replacing the phenolic moieties in **11**, **15**, and **19** with pyridin-2-yl in **9**, **13**, and **17** or pyridin-4-yl groups in **10**, **14**, and **18**, respectively decreased the ROS scavenging potency. It could be postulated that the proximity of the pyridinyl nitrogen to the oxadiazole core in the pyridin-2-yl derivatives compared to the pyridin-4-yl derivatives can offer, in most cases, relatively higher (or at least comparable) stability to the corresponding generated radical as exemplified by the enhanced ROS quenching activity of **13** relative to **14**. Deletion of the ring nitrogen i.e., substitution of the pyridinyl group with phenyl group afforded relatively less active derivatives **8**, **12**, and **16**. This may be attributed to losing the ROS quenching effect of the pyridinyl nitrogen. Replacing the aromatic ring at position 5 of the oxadiazole core in **18** and **19** with a

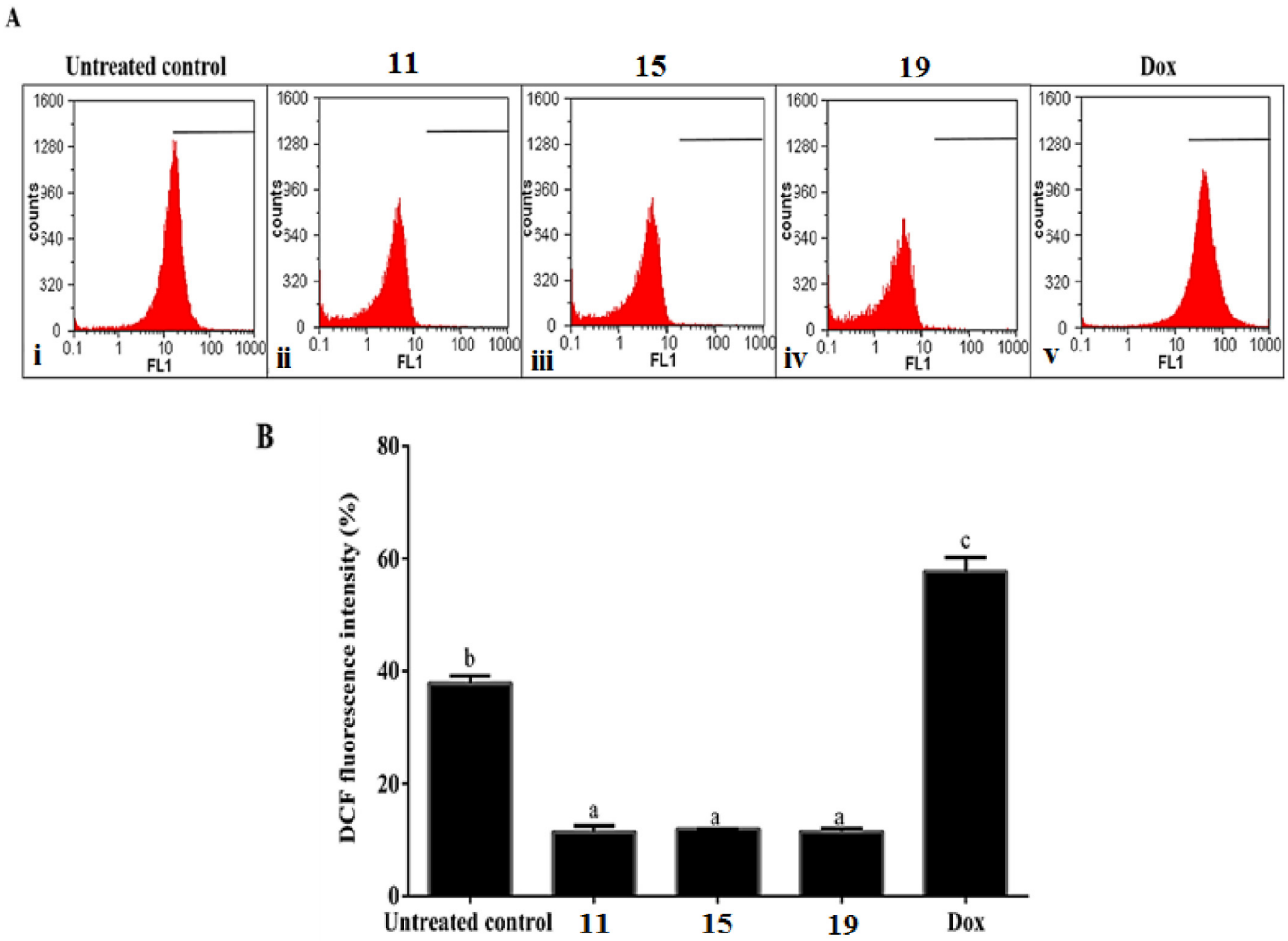

Fig. 4. (A) Flow charts of the level of the oxidized DCF (cellular ROS) in; **(i)** the untreated HepG-2 cells, **(ii) 11** (23.5 nM)-treated HepG-2 cells, **(iii) 15** (27.3 nM)-treated HepG-2 cells, **(iv) 19** (14.9 nM)-treated HepG-2 cells, and **(v)** DOX. (22 nM)-treated HepG-2 cells. **(B)** The relative oxidized DCF percentages.

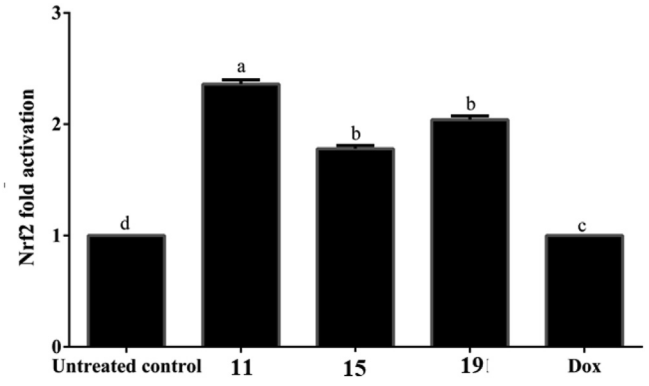

Fig. 5. Nrf2 activation by the evaluated oxadiazoles **11** (65.1 nM), **15** (45.4 nM) and **19** (72 nM) in the treated HepG-2 cells relative to DOX. (11.5 nM)-treated HepG-2 cells and untreated control. All values are expressed as mean ± SEM. Different letters are significantly different at $P < 0.05$.

methyl group in **20** decreased the free radical scavenging potency. This highlights the stabilizing effect of the aromatic ring on the corresponding formed radicals during the antioxidant process. Unexpectedly, this observation wasn't seen when comparing **20** with **16** and **17**, where the latter derivatives were relatively devoid

Table 3
In vitro TrxR1 inhibitory activities of the selected oxadiazoles **11**, **15**, and **19**.

Compound No.	IC_{50} (nM)	pIC_{50}[a]	LE[b]	LLE[c]	LELP[d]
11	13.19 ± 0.55	7.879	0.599	5.759	3.539
15	17.89 ± 1.11	7.747	0.558	5.647	3.763
19	9.21 ± 1.45	8.035	0.500	5.025	6.020
Staurosporine	43.18 ± 1.23	–	–	–	–

* All values are expressed as mean ± SEM.
[a] pIC_{50}: negative logarithm of half-maximal inhibitory concentration (in molar concentration).
[b] LE: ligand efficiency; representing the balance between potency and size [74,75].
[c] LLE: lipophilic ligand efficiency; a link between potency and lipophilicity [77,78].
[d] LELP: ligand efficiency-dependent lipophilicity index; a descriptor combining molecular size, lipophilicity, and potency into one composite [76].

of ROS scavenging potencies. Concerning the iron chelation activities, the phenolic derivatives **11**, **15**, and **19** were also the most efficient iron chelators among the series, where the 3-benzyl substituted oxadiazole **15** and the 3-trifluoromethylphenyl derivative **19** were comparable to EDTA. This could be correlated to the intrinsic iron chelation ability of the phenolic compounds [99]. Another SAR was deduced when comparing the iron chelation potency of remainder 1,2,4-oxadiazoles substituted with pyridinyl groups namely, **9**, **10**, **13**, **14**, **17** and **18,** to their phenyl analogs 8, **12**,

Table 4
In vitro IKKα inhibitory activities of the selected oxadiazoles **11**, **15**, and **19**.

Compound No.	IC_{50} (nM)	pIC_{50}	LE	LLE	LELP
11	11.00 ± 0.31	7.958	0.605	5.838	3.504
15	15.94 ± 0.45	7.795	0.562	5.695	3.736
19	10.58 ± 0.30	7.975	0.496	4.965	6.068
Staurosporine	62.60 ± 0.17	–	–	–	–

* All values are expressed as mean ± SEM.

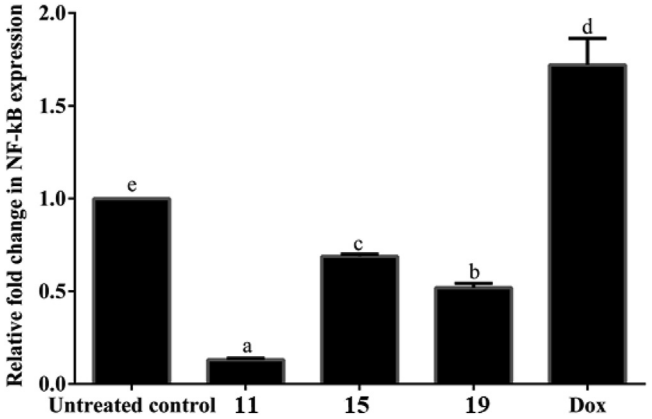

Fig. 6. Relative changes in the expression level of NF-kB in HepG-2 cells after treatment with IC_{50} doses of **11** (23.5 nM), **15** (27.3 nM), **19** (14.9 nM), and DOX. (22 nM) compared to untreated cells for 72 h. All values are expressed as mean ± SEM. Different letters are significantly different at $P < 0.05$.

Table 5
In vitro NADPH oxidase inhibitory activities of the selected oxadiazoles **11**, **15**, and **19**.

Compound No.	IC_{50} (nM)	pIC_{50}	LE	LLE	LELP
11	16.40 ± 0.46	7.785	0.592	5.665	3.581
15	21.94 ± 0.62	7.658	0.552	5.558	3.804
19	10.71 ± 0.30	7.970	0.496	4.960	6.068
Staurosporine	70.77 ± 0.20	–	–	–	–

* All values are expressed as mean ± SEM.

and **16**. Obviously, the pyridinyl substituted derivatives were more efficient than the corresponding phenyl substituted ones. This is in accordance with previous studies reporting possible formation of heavy metal complexes of oxadiazoles with various nitrogenous heterocycles [100] Cytotoxicity screening revealed that the three phenolic derivatives **11**, **15**, and **19** exhibited good safety profiles on normal cells and excellent anticancer activities even superior to the reference chemotherapeutic agent; doxorubicin on all the screened cell lines. These results were in accordance with the preliminary *in vitro* antioxidant evaluation. It is worth mentioning that various studies highlighted the correlation between antioxidant activities of the phenolic compounds and their cytoprotective/anticancer potencies [99,101,102]. The 3-trifluoromethylphenyl and the unsubstituted phenyl groups conferred comparable anticancer potencies to **19** and **11**, respectively against MDA-MB231 cells, followed by the slightly less active 3-benzyl derivative **15**. Higher selectivity was detected against HepG-2 and Caco-2 cells, where the 3-trifluoromethylphenyl substituted oxadiazole **19** was the most promising among the series followed by the 3-phenyl derivative **11** and the slightly less active 3-benzyl analog **15**. Obviously, other substitutions did not offer similar or higher safety profiles together with broad anticancer activities. Further investigation of the intracellular ROS scavenging potential of the selected three phenolic oxadiazoles **11, 15,** and **19** in HepG-2 cells showed that they were nearly equipotent. Mechanistic studies showed that the 3-phenyl substitution in **11** had the highest potential to activate Nrf2 in HepG-2 cells, followed by the trifluoromethylphenyl group in **19** and the 3-benzyl group in **15**. A similar pattern was observed when assaying the activity of the studied derivatives on NF-κB signaling. However, the 3-trifluoromethyl phenyl substitution in **19** endowed the highest TrxR1, IKKα, and NADPH oxidase inhibition, closely followed by the unsubstituted phenyl in **11** and the 3-benzyl moiety in **15**. Taken together, it seems that the enhanced NF-κB downregulation potential of **11** relative to the other derivatives besides the detected minor differences between the enzymatic inhibitory activities of the three derivatives, especially between **11** and **19**, might have endowed relatively higher Nrf2 activation to **11**, however it is still comparable to **19**.

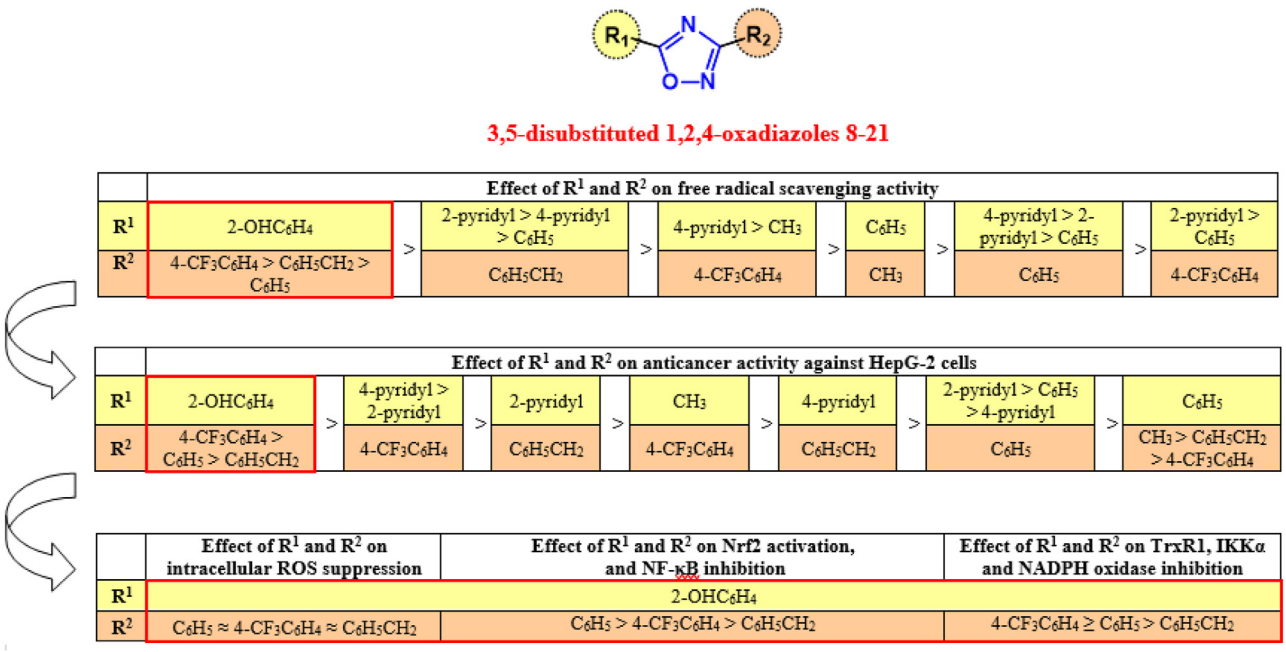

Fig. 7. SAR of the synthesized 3,5-disubstituted 1,2,4-oxadiazoles **8**–**21**.

3.4. Molecular modeling studies

3.4.1. Docking

Docking simulations were performed by MOE 2015.10 [103] to enrich the deduced structure-activity relationship with reasonable explanations, predict the probable binding modes of the active oxadiazole derivatives into the evaluated enzymes active sites, and possibly justify the adopted design strategy.

3.4.1.1. Docking of the active oxadiazoles (11, 15, and 19) into TrxR. Mammalian TrxR contains a unique carboxyl-terminal Gly-Cys-SeCys-Gly motif that is essential for its catalytic activity [104]. Mechanistic studies showed that the enzyme is irreversibly inhibited by dinitrohalobenzenes that can interact with both the redox-active selenocysteine and its neighboring cysteine [105]. In this study, the crystal structure of mammalian TrxR with the co-factors FAD and NADP was retrieved from the protein data bank (PDB ID: 1h6v [104]). The dimer formed of E and F chains was considered due to the presence of more solved residues of EF subunits compared to AB and CD [106]. Unwanted residues, ligands, and solvents were eliminated then the dimer was prepared employing the "QuickPrep" module with default settings. The three-dimensional structure of the site containing the redox-active SeCys498Cys sequence was located utilizing the 'Site Finder' feature of MOE 2015.10. Structures of the studied oxadiazoles **11, 15**, and **19** were built *in silico* and subjected to default energy minimization and geometry optimization. Docking was conducted with induced fitting protocol to record the best docking scores and molecular interactions. The best binding modes of the investigated derivatives (Fig. 8) were nearly correlated with their *in vitro* TrxR inhibition profiles (Table 3), where **19** was slightly more active than **11** and 2-fold more potent than **15** (Table 3). Obviously, Cys498 of the C-terminal tail interacted with the oxadiazole core nitrogen of **11** and **19** *via* hydrogen bonds of nearly similar length (3.25 and 3.58 Å, respectively). Interestingly, this observation agreed with our design rationale. The poses recorded good free binding energies (−5.10 and −5.07 kcal/mol, respectively) at RMSD ˂ 2. On the other hand, the less active 3-benzyl oxadiazole derivative **15** failed to display these interactions but recorded similar free binding energy (−5.09 kcal/mol). This encourages further research on the designed 1,2,4-oxadiazole scaffold for gaining more information on the substitutes exhibiting important interactions with the Gly-Cys-SeCys-Gly motif that probably will allow enhanced TrxR inhibitory activity.

3.4.1.2. Docking of the active oxadiazoles (11, 15, and 19) into IKKα active site. The non-canonical NF-κB-signaling depends on IKK1/α [107]. The human IKK1 X-ray crystal structure (PDB ID: 5EBZ [108]) was detected as a hexamer in the presence of the Calbiochem IKK inhibitor XII [109]. The IKK1 hexamer is a trimer of dimers. In the current study, the crystal structure of Human IKK1 was retrieved from the protein data bank (PDB ID: 5EBZ [108]). After eliminating unwanted residues, ligands, and solvents, the IKK1 monomer was prepared utilizing the default "QuickPrep" module. Structures of the active oxadiazoles **11**, **15**, and **19** were built *in silico*, subjected to default energy minimization, and flexibly docked into the co-crystallized inhibitor's binding site. As illustrated (Fig. 9), the most active oxadiazoles **11** and **19** shared some key H-bond interactions (Cys98 and Glu19) with the reference IKK inhibitor. Interestingly, the phenolic hydroxyl groups of **11** and **19** offered these H-bonding interactions at nearly similar distances (2.9 Å) to those displayed by the co-crystallized IKK inhibitor (2.8 Å). The oxadiazole core of **11** exhibited H-π interactions (4.36 Å) with the receptor Asp102, whereas shorter H-π interactions (3.64 Å) were shown between the trifluoromethylphenyl moiety of **19** and Leu21. On the other hand, the least active derivative among the evaluated group **15** missed the co-crystallized ligand interactions. However, the best binding modes of **15** recorded more favorable free binding energy (−6.28 kcal/mol) than those displayed by **11** and **19** (−5.56 and −5.69 kcal/mol, respectively). This may provide an explanation to the detected relatively slight differences between their *in vitro* IC_{50} values (Table 4). Based on these observations, it could be postulated that the proximity of the oxadiazole core with respect to the aromatic moieties allowed favorable interactions with the IKKα active site.

3.4.1.3. Docking of the active oxadiazoles (11, 15, and 19) into NADPH oxidase. NADPH oxidase is identified as a multimeric enzyme that consists of gp91phox (renamed as Nox2), p22phox, three cytosolic subunits (p40phox, p47phox, and p67phox), and the small G-proteins (Rap1A and Rac1/2) [110,111]. NADPH oxidase mutations studies suggested that p47phox requires at least three serines for oxidase activation namely; Ser379, phosphorylated Ser303 or Ser304, and phosphorylated Ser 359 or Ser370 [112]. Additionally, various studies have been conducted to predict the possible interactions between NADPH oxidase and its inhibitors. The potential active site was not clear, except for some key amino acid residues. Among these, Cys378 was accepted as a key residue directly related to the inhibitory activities [113–116]. Accordingly, the potential NADPH oxidase active site was previously identified as the pocket containing Cys378 by the Site ID program of Sybyl7.0 applying the flood-fill solvation technique [117]. Herein, the 3D structure of NADPH oxidase consisting of the C-terminal SH3 domain of p67phox complexed with the C-terminal tail region of p47phox was derived from the protein data bank (PDB ID: 1K4U [118]) and prepared employing the "QuickPrep" module of MOE 2015.10. with default settings. The 'Site Finder' feature was then used to seek all the possible pockets considering the key amino acids (Cys378 and Ser379). Oxadiazoles **11, 15,** and **19** were built *in silico*, subjected to the default geometry optimization protocols, and docked into the selected potential active site. Docking simulation results (Fig. 10) showed that the phenolic hydroxyl groups of the most active derivatives **11** and **19** offered H-bonding interactions of similar lengths (3 Å) with Ser379. On the other hand, the less active oxadiazole **15** missed considerable interactions. Besides, **11** and **19** recorded more favorable binding energies (−4.62 and −4.95 kcal/mol, respectively) than **15** (−4.50 kcal/mol). These observations were nearly consistent with NADPH oxidase inhibition profiles of the investigated oxadiazoles, where **19** and **11** were more potent than **15** (Table 5). Based on these results, it may be predicted that the phenolic hydroxyl group participate in important interactions with NADPH oxidase that will probably add to the intrinsic antioxidant activity of the 1,2,4-oxadiazole scaffold. This observation paves the road to further computational studies for better understanding of the SAR governing 1,2,4-oxadiazole-based NADPH oxidase inhibitors.

3.4.2. In silico prediction of physicochemical properties, ADMET and drug-likeness parameters

Recently, the medicinal chemistry research programs involve *in silico* prediction studies of physicochemical properties, ADMET, and drug-likeness parameters as useful lead identification tools. Herein, the physicochemical properties formulating various drug-likeness parameters were computed for all the studied oxadiazoles utilizing *SwissADME* [119] software (Table 6). Interestingly, not only the most active derivatives (**11**, **15**, and **19**), but also all the synthesized oxadiazoles showed drug-like bioavailability prediction according to Lipinski's [120], Veber's [121], and Muegge's [122] parameters, except for **21** regarding Muegge's parameters. *Molsoft* software [66] predicted excellent aqueous solubility for almost all the

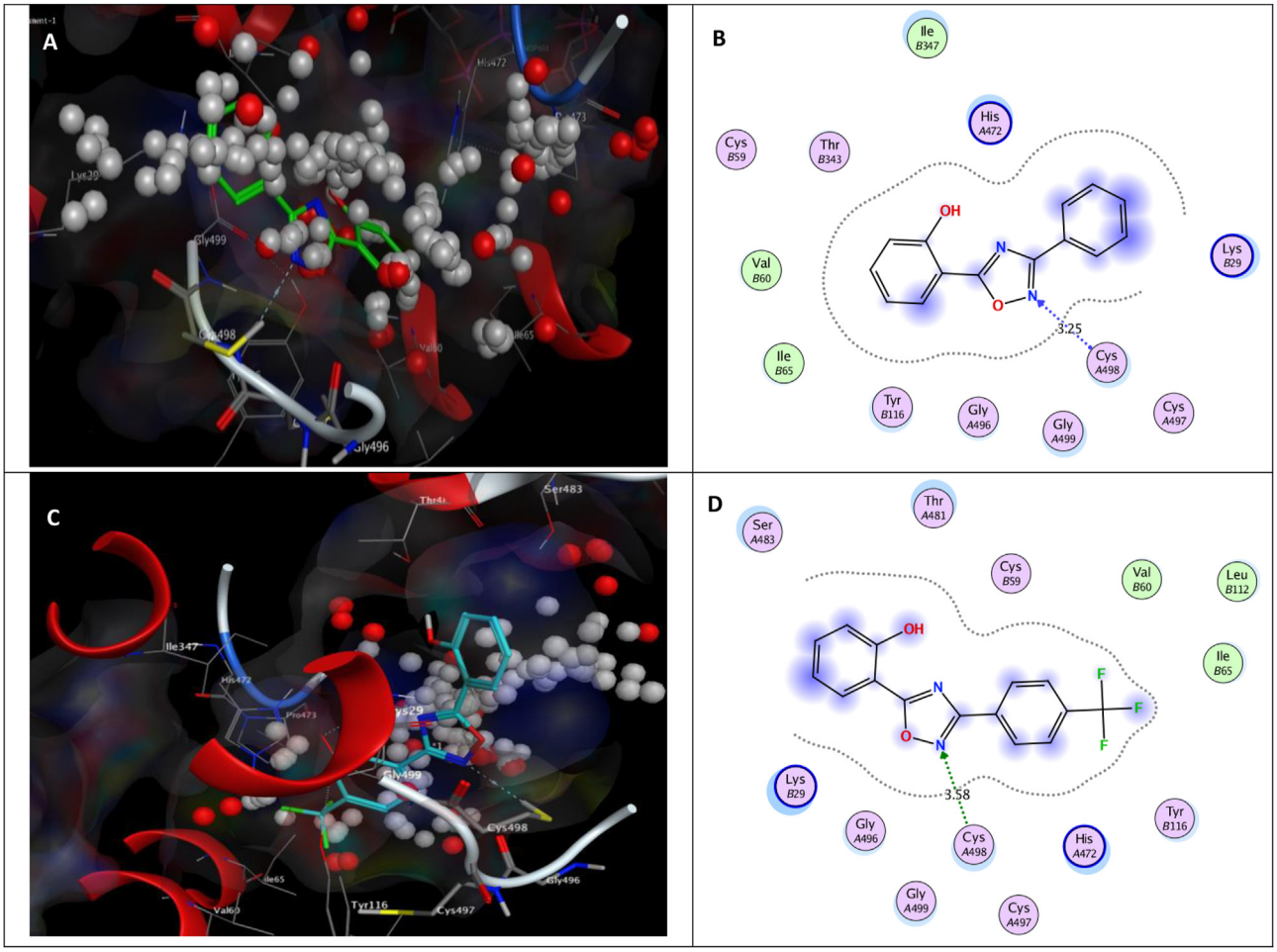

Fig. 8. (A) 3D binding mode of **11** (green sticks), **(B)** 2D binding mode of **11**, **(C)** 3D binding mode of **19** (cyan sticks), and **(D)** 2D binding mode of **19**, in the redox-active site of TrxR (PDB ID: 1h6v).

investigated compounds. Moreover, *Pre-ADMET* software [91] was employed for ADME prediction. All compounds were predicted to have high intestinal absorption (>95%), medium to high CNS absorption, medium Caco2 model permeability values, low to medium MDCK model ones, and weak plasma proteins binding (except **8**, **12**, and **14)** indicating that much of the unbound compound will be available for transport across various membranes. They were predicted to be devoid of cytochromes P450 2D6 (CYP2D6) inhibition activities but not CYP3A4. PROTOX [123], the toxicity predictor program, predicted the average lethal dose (LD_{50}) of the studied oxadiazoles in rodents and classified it according to the Globally Harmonized System of Classification and Labeling of Chemicals (GHS) as class IV concerning acute oral toxicity. **11, 15,** and **19** were predicted to be the safest among the group and could be considered druggable.

4. Conclusion

This study investigates the potential of rationally designed 1,2,4-oxadiazole derivatives to target Nrf2 negative modulators; TrxR, IKK, and NF-κB, thus indirectly activating Nrf2 for treating cancer. Among the evaluated series, the phenolic derivatives **11, 15**, and **19** exhibited the highest ROS scavenging (≈L-ascorbic acid) and iron chelating activities (≈EDTA). They suppressed ROS in HepG-2 cells by 3 folds, *in vitro* inhibited TrxR1, IKKα, and NADPH oxidase at nanomolar IC_{50} doses, and downregulated NF-kB in HepG-2 cells by 7.6, 1.4, and 1.9 folds, respectively. Hence, they activated Nrf2 in HepG-2 cells by 2.36, 1.78, and 2.04 folds, respectively. This antioxidant potential possibly contributed to their promising anticancer potencies, where they were superior to reference chemotherapy against HepG-2, MDA-MB231, and Caco-2 cells. Docking simulations predicted their binding modes with TrxR1, IKKα, and NADPH oxidase and explained SAR, particularly the possible contribution of the phenolic groups to their binding affinities. This highlighted the importance of the phenolic 1,2,4-oxadiazole derivatives that deserve further investigation. Finally, they were *in silico* predicted to possess drug-like physicochemical parameters, ADMET, and ligand efficiency metrics.

5. Experimental

5.1. Chemistry

5.1.1. Materials and equipment

All reactions were carried out in dried glassware. NMR spectra were measured using a JEOLJNM ECA 500 or 400. The deuterated solvent was used as an internal deuterium lock. ^{13}C NMR spectra were recorded using the UDEFT pulse sequence and broad band proton decoupling at 100 or 125 MHz. All chemical shifts (δ) are stated in units of parts per million (ppm) and presented using TMS as the standard reference point. Mass spectra were recorded on direct probe controller inlet part to single quadropole mass

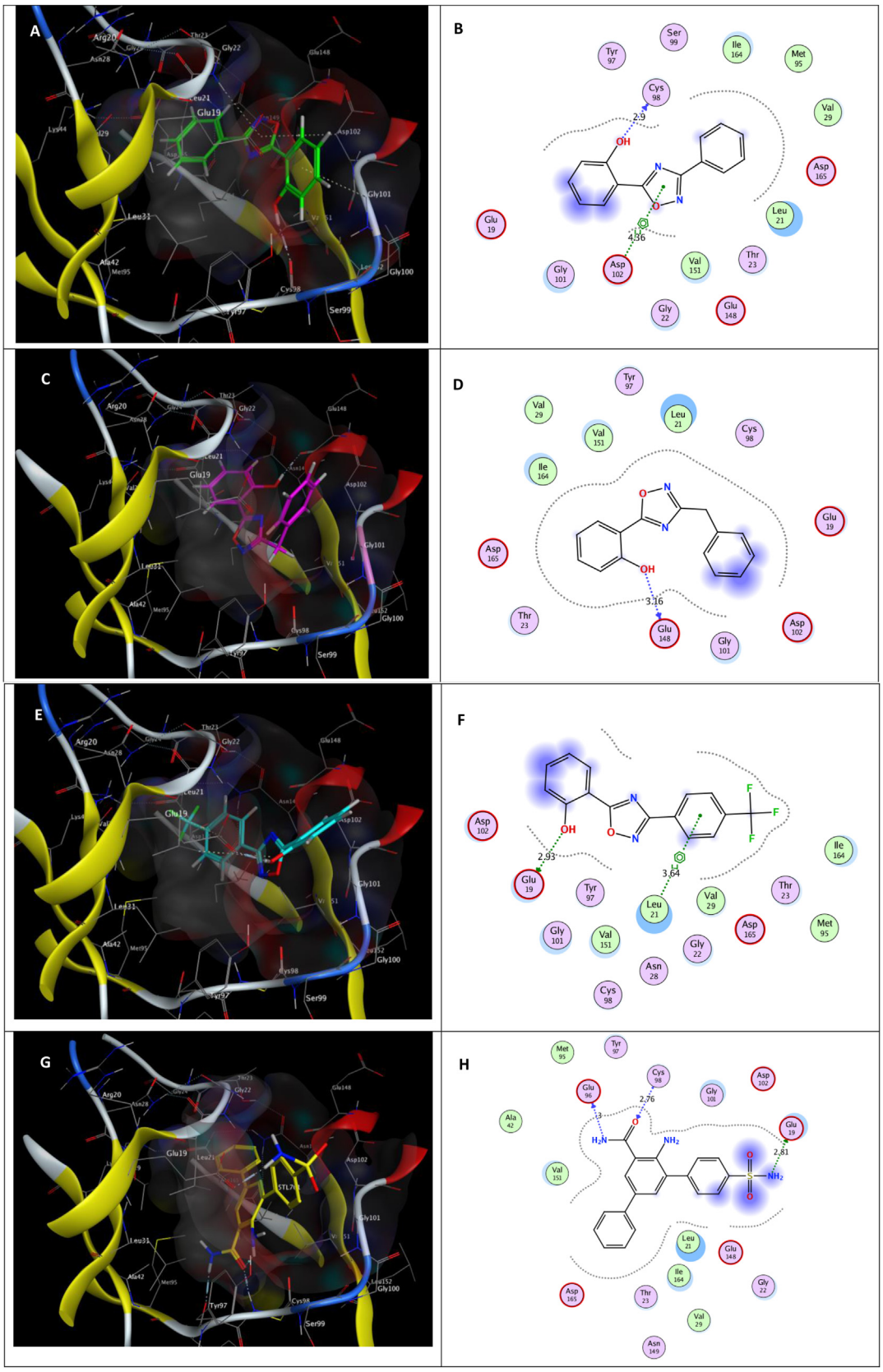

Fig. 9. (A) 3D binding mode of **11** (green sticks), **(B)** 2D binding mode of **11**, **(C)** 3D binding mode of **15** (magenta sticks), **(D)** 2D binding mode of **15**, **(E)** 3D binding mode of **19** (cyan sticks), **(F)** 2D binding mode of **19**, **(G)** 3D binding mode of IKK inhibitor XII (yellow sticks), and **(H)** 2D binding mode of IKK inhibitor XII in the co-crystallized inhibitor binding site of IKK1/α (PDB ID: 5EBZ).

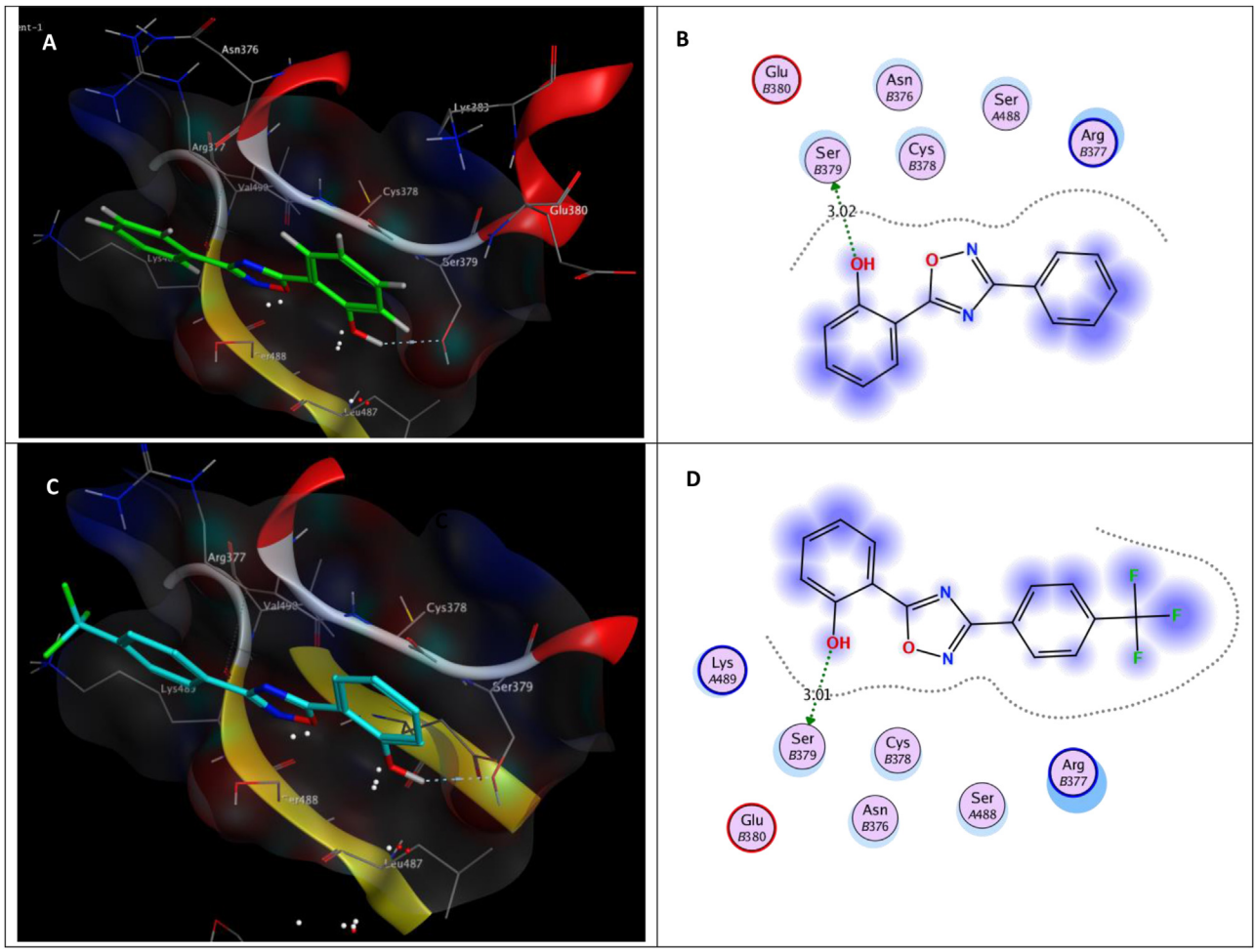

Fig. 10. (A) 3D binding mode of **11** (green sticks), **(B)** 2D binding mode of **11**, **(C)** 3D binding mode of **19** (cyan sticks), and **(D)** 2D binding mode of **19**, in NADPH oxidase (PDB ID: 1K4U) active site.

analyzer in Thermo Scientific EIMS, Model: ISQ LT, using thermo x-Calibur software. Values are reported as the ratio of mass to charge (*m*/*z*) in Daltons. Melting points were recorded using Thermo Scientific, Model NO: 1002D, 220-240v; 200 W; 50/60 Hz and are uncorrected. IR (KBr) ν_{max} (cm^{-1}) data were recorded using PerkinElmer; FT-IR Spectrum BX and Bruker tensor 37 FT-IR. Reaction time was monitored by TLC on Merck silica gel aluminum cards (0.2 mm thickness) with a fluorescent indicator at 254 nm. Visualization of the TLC during monitoring of the reaction was done by UV VILBER LOURMAT 4w-365 nm or 254 nm tube.

5.1.2. General procedure for the synthesis of 3,5-disubstituted 1,2,4-oxadiazoles (8–21)

To a solution of amidoxime **2a-d** (1.0 mmol) and carboxylic ester **3**–**7** (1.5 mmol) in DMSO (2 mL), 80 mg (2.0 mmol) of powdered NaOH was rapidly added. The reaction mixture was stirred at room temperature for the required time. After completion of the reaction, as indicated by TLC, the reaction mixture was diluted with cold water (30–50 mL). The resulting precipitate was filtered off, washed with water (30 mL), and recrystallized from ethanol [81]. For the phenolic derivatives **11**, **15**, and **19**, the reaction was carried out as mentioned. After completion, the reaction mixture was diluted with cold water (30–50 mL), neutralized to pH = 2 using HCl (6.0 M). The resulting precipitate was filtered off, washed with water (30 mL), and recrystallized from ethanol.

5.1.2.1. 3,5-Diphenyl-1,2,4-oxadiazole (8). Yield 80% (178 mg), as a white solid: m.p = 107–108 °C (lit [129]. m.p = 107–109 °C); IR (KBr) ν_{max} (cm^{-1}) 3487, 3435, 2094, 1824, 1774, 1634, 1563, 1446, 1365, 1271, 1160, 727; **^{1}H NMR** (500 MHz, $CDCl_3$) δ_H: 8.14–8.08 (m, 4H, Ar–**H**), 7.54–7.48 (m, 6H, Ar–**H**); **^{13}C NMR** (125 MHz, $CDCl_3$) δ_C: 175.7, 168.8 (oxadiazole-**C**),132.6, 131.1, 129.0, 128.8, 128.1, 127.4, 126.9, 124.2; EIMS *m*/*z* $[M]^+$ calcd for $[C_{14}H_{10}N_2O]^+$: 222.07, found 222.05; Anal. Calcd for $C_{14}H_{10}N_2O$: C, 75.66; H, 4.54; N, 12.60. Found: C, 75.31; H, 4.72; N, 12.29.

5.1.2.2. 3-Phenyl-5-(pyridin-2-yl)-1,2,4-oxadiazole (9). Yield 77% (172 mg), as a white solid: m.p = 115–116 °C (lit [130]. m.p =116 °C); IR (KBr) ν_{max} (cm^{-1}) 3473, 3415, 3054, 2853, 2032, 1822, 1623, 1588, 1472, 1361, 1132, 733;**^{1}H NMR** (400 MHz, $CDCl_3$) δ_H: 8.80 (d, *J* = 4.5 Hz, 1H, Py -**H**), 8.24 (d, *J* = 10 Hz, 1H, Py -**H**), 8.16 (d, *J* = 8.5 Hz, 2H, Ar–**H**), 7.87 (t, 1H, *J* = 10.5 Hz, Py -**H**), 7.48–7.43 (m, 4H, Ar–**H,** Py -**H**); **^{13}C NMR** (100 MHz, $CDCl_3$) δ_C: 174.5, 169.2 (oxadiazole-**C**), 150.7, 143.6, 137.3 (Py -**C),** 131.3, 128.8, 127.6, 126.6, 126.5, 124.1 (Ar–**C,** Py -**C);** EIMS *m*/*z* $[M]^+$ calcd for $[C_{13}H_9N_3O]^+$: 223.07, found 223.18; Anal. Calcd for $C_{13}H_9N_3O$: C, 69.95; H, 4.06; N, 18.82. Found: C, 70.24; H, 4.31; N, 19.05.

5.1.2.3. 3-Phenyl-5-(pyridin-4-yl)-1,2,4-oxadiazole (10). Yield 74% (166 mg), as a white solid: m.p = 160–162 °C; IR (KBr) ν_{max} (cm^{-1}) 3421, 3033, 2854, 1938, 1577, 1544, 1448, 1363, 1133, 835, 733; **^{1}H**

Table 6
In silico predicted physicochemical properties, ADMET and drug-likeness parameters of 3,5-disubstituted 1,2,4-oxadiazoles **8**–**21**.

Compound No.	Physicochemical parameters							ADMET								Drug-likeness		
	Log P[a]	M.Wt[b]	HBA[c]	HBD[d]	NROTB[e]	TPSA[f]	S[g]	HIA[h]	PPB[i]	BBB[j]	Caco2[k]	MDCK[l]	CYP3A4 inhibitor	CYP2D6 inhibitor	LD_{50}[m]	Lipiniski[n]	Veber[o]	Muegge[p]
8	3.11	222.24	3	0	2	38.92	12.53	98.21	90.16	3.86	43.21	24.93	Yes	No	1000	Yes	Yes	Yes
9	1.99	223.23	4	0	2	51.81	168.95	98.21	89.55	1.97	39.62	340.57	Yes	No	1000	Yes	Yes	Yes
10	1.99	223.23	4	0	2	51.81	206.22	98.21	79.16	0.016	33.42	61.48	Yes	No	1000	Yes	Yes	Yes
11	**2.12**	**238.24**	**4**	**1**	**2**	**59.15**	**26.20**	**95.66**	**88.07**	**1.38**	**19.75**	**38.34**	**Yes**	**No**	**2000**	**Yes**	**Yes**	**Yes**
12	3.09	236.27	3	0	3	38.92	47.47	98.14	91.84	3.89	47.67	23.51	Yes	No	1270	Yes	Yes	Yes
13	1.99	237.26	4	0	3	51.81	407.28	98.17	82.91	0.07	40.23	50.15	Yes	No	1270	Yes	Yes	Yes
14	1.99	237.26	4	0	3	51.81	814.37	98.17	91.11	1.70	44.12	347.24	Yes	No	1270	Yes	Yes	Yes
15	**2.10**	**252.27**	**4**	**1**	**3**	**59.15**	**87.07**	**95.68**	**88.10**	**1.29**	**21.39**	**24.12**	**Yes**	**No**	**2000**	**Yes**	**Yes**	**Yes**
16	4.00	290.24	6	0	3	38.92	1.23	98.13	88.43	0.06	26.41	0.18	Yes	No	1000	Yes	Yes	Yes
17	2.90	291.23	7	0	3	51.81	12.61	98.16	87.33	0.02	23.61	0.40	Yes	No	1000	Yes	Yes	Yes
18	2.90	291.23	7	0	3	51.81	13.80	98.16	84.35	0.04	23.41	2.57	Yes	No	1000	Yes	Yes	Yes
19	**3.01**	**306.24**	**7**	**1**	**3**	**59.15**	**7.58**	**95.68**	**88.17**	**0.12**	**21.45**	**0.07**	**Yes**	**No**	**2000**	**Yes**	**Yes**	**Yes**
20	2.26	228.17	6	0	2	38.92	78.55	98.50	61.51	2.61	23.68	46.32	Yes	No	1000	Yes	Yes	Yes
21	1.66	160.17	3	0	1	38.92	2405.26	98.32	68.96	1.73	30.96	59.57	Yes	No	1000	Yes	Yes	No

[a] Log P: logarithm of compound partition coefficient between *n*-octanol and water.
[b] M.Wt: molecular weight.
[c] HBA: number of hydrogen bond acceptors.
[d] HBD: number of hydrogen bond donors.
[e] NROTB: number of rotatable bonds.
[f] TPSA: polar surface area. Drug-like TPSA <140–150 A^2.
[g] S: aqueous solubility (mg/L).
[h] HIA: human intestinal absorption. HIA values < 20% (poorly absorbed), values ≈ 20–70% (moderately absorbed) and values > 70% (well absorbed) [124].
[i] PPB: plasma protein binding. PPB values < 90% (poorly bound) and values > 90% (strongly bound) [91].
[j] BBB: blood-brain barrier penetration. BBB values < 0.1 (low CNS absorption), values ≈ 0.1–2 (medium CNS absorption) and values > 2 (high CNS absorption) [125].
[k] Caco2: permeability through cells derived from human colon adenocarcinoma. PCaco2 values < 4 nm/s (low permeability), values ≈ 4–70 nm/s (medium permeability) and values > 70 nm/s (high permeability) [126–128].
[l] MDCK: permeability through Madin-Darby Canin kidney cells. PMDCK values < 25 nm/s (low permeability), values ≈ 25–500 nm/s (medium permeability) and values > 500 nm/s (high permeability) [127].
[m] LD50: the median lethal dose (mg/Kg). Toxicity classes according to GHS are: Class I: fatal if swallowed (LD50 ≤ 5), Class II: fatal if swallowed (5 < LD50 ≤ 50), Class III: toxic if swallowed (50 < LD50 ≤ 300), Class IV: harmful if swallowed (300 < LD50 ≤ 2000), Class V: may be harmful if swallowed (2000 < LD50 ≤ 5000), and Class VI: non-toxic (LD50 > 5000) [123].
[n] Lipinski rule: log P ≤ 5, M.Wt ≤ 500 Da, HBA ≤10 and HBD ≤5 [120].
[o] Veber rule: NROTB ≤10 and TPSA ≤140 [121].
[p] Muegge rule: 2 ≤ log P ≤ 5, 200 ≤ M.Wt ≤ 500 Da, TPSA ≤150, Num. rings ≤7, Num. carbons >4, Num. heteroatom >1, NROTB ≤15, HBA ≤10 and HBD ≤5 [122].

NMR (500 MHz, DMSO-d_6) δ_H: 8.90 (dd, J = 4.5 Hz, 1.5 Hz, 2H, Py -**H**), 8.10–8.08 (m, 4H, Ar–**H,** Py -**H**), 7.65–7.58 (m, 3H, Ar–**H**); **^{13}C NMR** (125 MHz, DMSO-d_6) δ_C: 173.9, 168.5 (oxadiazole-**C**), 151.2 (Py -**C**), 131.9, 130.3, 129.4, 127.1, 125.7, 121.3 (Ar–**C**); EIMS m/z $[M]^+$ calcd for $[C_{13}H_9N_3O]^+$: 223.07, found 223.01 Anal. Calcd for $C_{13}H_9N_3O$: C, 69.95; H, 4.06; N, 18.82. Found: C, 70.20; H, 4.42; N, 18.95.

5.1.2.4. 2-(3-Phenyl-1,2,4-oxadiazol-5-yl)phenol (11). Yield 59% (141 mg), as a white solid: m.p = 158–159 °C; IR (KBr) ν_{max} (cm^{-1}) 3471, 3415, 3039, 2963, 2927, 1965, 1808, 1614, 1544, 1459, 1362, 1113, 914, and 740; **^{1}H NMR** (500 MHz, DMSO-d_6) δ_H: 10.57 (s, 1H, OH exchangeable with D_2O), 8.08 (dd, J = 7.5 Hz, 1.5 Hz, 2H,Ar–**H**), 7.98 (dd, J = 7.5 Hz, 1.5 Hz, 1H, Ar–**H**), 7.60–7.56 (m, 3H, Ar–**H**), 7.50 (td, J = 8.5 Hz, 2 Hz, 1H, Ar–**H**), 7.10 (d, J = 8.5 Hz, 1H, Ar–**H**), 7.01 (t, J = 7.5 Hz, 1H, Ar–**H**); **^{13}C NMR** (125 MHz, DMSO-d_6) δ_C: 175.0, 167.2 (oxadiazole-**C**), 157.2, 134.8, 131.6, 130.0, 129.2, 127.1, 126.0, 119.7, 117.4, 109.7 (Ar–**C**); EIMS m/z $[M]^+$ calcd for $[C_{14}H_{10}N_2O_2]^+$: 238.07, found 238.54; Anal. Calcd for $C_{14}H_{10}N_2O_2$: C, 70.58; H, 4.23; N, 11.76. Found: C, 70.37; H, 4.41; N, 11.51.

5.1.2.5. 3-Benzyl-5-phenyl-1,2,4-oxadiazole (12). Yield 70% (164 mg), as a white solid: m.p = 82–83 °C (lit [131]. m.p = 82–84 °C); IR (KBr) ν_{max} (cm^{-1}) 3432, 3061, 3030, 2963, 2930, 2251, 1967, 1821, 1771, 1609, 1557, 1509, 1484, 1361, 1272, 1104, 997, 833, 725; **^{1}H NMR** (500 MHz, $CDCl_3$) δ_H: 8.01 (d, J = 10 Hz, 2H, Ar–**H**), 7.44–7.17 (m, 8H, Ar–**H**), 4.06 (s, 2H, PhC**H**$_2$); **^{13}C NMR** (125 MHz, DMSO-d_6) δ_C: 175.0, 169.9 (oxadiazole-**C**), 135.7, 133.2, 129.5, 128.9, 128.5, 127.7, 126.9, 123.3, (Ar–**C**), 31.4 (Ph**C**H$_2$); EIMS m/z $[M]^+$ calcd for $[C_{15}H_{12}N_2O]^+$: 236.09, found 236.42; Anal. Calcd for $C_{15}H_{12}N_2O$: C, 76.25; H, 5.12; N, 11.86. Found: C, 76.51; H, 5.37; N, 11.62.

5.1.2.6. 3-Benzyl-5-(pyridin-2-yl)-1,2,4-oxadiazole (13). Yield 58% (138 mg), as a white solid: m.p = 74–76 °C; IR (KBr) ν_{max} (cm^{-1}): 3549, 3475, 3415, 3026, 2928, 2246, 1963, 1887, 1802, 1615, 1572, 1443, 1363, 1308, 1285, 1073, and 734; **^{1}H NMR** (500 MHz, DMSO-d_6) δ_H: 8.76 (d, J = 4.0 Hz, 1H, Py -**H**), 8.16 (d, J = 7.5 Hz, 1H, Py -**H**), 8.02 (td, J = 7.5 Hz, 2.0 Hz, 1H, Py -**H**), 7.65 (t, 1H, J = 7.0 Hz, Py -**H**), 7.33–7.29 (m, 4H, Ar–**H**),7.24–7.21 (m, 1H, Ar–**H**),4.17 (s, 2H, PhC**H**$_2$); **^{13}C NMR** (125 MHz, DMSO-d_6) δ_C: 174.1, 170.1 (oxadiazole-**C**), 150.5, 142.7, 138.0, 135.6 (Py -**C**),128.9, 128.6, 127.4, 126.9, 124.3 (Ar–**C,** Py -**C**),31.4 (Ph**C**H$_2$); EIMS m/z $[M]^+$ calcd for $[C_{14}H_{11}N_3O]^+$: 237.09, found 237.28; Anal. Calcd for $C_{14}H_{11}N_3O$: C, 70.87; H, 4.67; N, 17.71. Found: C, 70.91; H, 4.76; N, 17.88.

5.1.2.7. 3-Benzyl-5-(pyridin-4-yl)-1,2,4-oxadiazole (14). Yield 65% (152 mg), as a white solid: m.p = 86–88 °C; IR (KBr) ν_{max} (cm^{-1}):3415, 3039, 2963, 2927, 1965, 1808, 1614, 1544, 1459, 1362, 1113, 914, and 740; **^{1}H NMR** (500 MHz, DMSO-d_6) δ_H: 8.84 (dd, J = 5.0 Hz, 2 Hz, 2H, Py -**H**), 7.98 (dd, J = 5.0 Hz, 2 Hz, 2H, Py -**H**), 7.35–7.33 (m, 4H, Ar–**H**), 7.25–7.24 (m, 1H, Ar–**H**), 4.21 (s, 2H, PhC**H**$_2$); **^{13}C NMR** (125 MHz, DMSO-d_6) δ_C: 173.5, 170.3 (oxadiazole-**C**), 151.1 (Py -**C**), 135.5, 130.3, 128.9, 128.6, 128.0, 127.0, 121.2 (Ar–**C,** Py -**C**),31.3 (Ph**C**H$_2$); EIMS m/z $[M]^+$ calcd for $[C_{14}H_{11}N_3O]^+$: 237.09, found 237.90; Anal. Calcd for $C_{14}H_{11}N_3O$: C, 70.87; H, 4.67; N, 17.71. Found: C, 70.48; H, 4.88; N, 17.52.

5.1.2.8. 2-(3-Benzyl-1,2,4-oxadiazol-5-yl)phenol (15). Yield 60% (142 mg), as a white solid: m.p = 90–91 °C; IR (KBr) ν_{max} (cm^{-1}): 3415, 3174, 3030, 2929, 2861, 1960, 1809, 1660, 1627, 1590, 1551, 1479, 1319, 1243, 1028, and 704; **^{1}H NMR** (500 MHz, DMSO-d_6) δ_H: 10.57 (s, 1H, OH exchangeable with D_2O), 7.90 (dd, J = 10.0 Hz, 1.5 Hz, 1H, Ar–**H**), 7.51 (td, J = 10.5 Hz, 2.0 Hz, 1H, Ar–**H**), 7.36–7.26 (m, 5H, Ar–**H**), 7.10 (d, J = 10.5 Hz, 1H, Ar–**H**), 7.01 (t, J = 9.5 Hz, 1H, Ar–**H**), 4.19 (s, 2H, PhC**H**$_2$); **^{13}C NMR** (125 MHz, DMSO-d_6) δ_C: 174.9, 169.3 (oxadiazole-**C**), 157.5, 136.2, 135.1, 130.2, 129.4, 129.0, 127.4, 120.2, 117.8, 110.1 (Ar–**C**), 31.7 (Ph**C**H$_2$); EIMS m/z $[M]^+$ calcd for $[C_{15}H_{12}N_2O_2]^+$: 252.08, found 252.53; Anal. Calcd for $C_{15}H_{12}N_2O_2$: C, 71.42; H, 4.79; N, 11.10. Found: C, 71.80; H, 4.91; N, 11.29.

5.1.2.9. 5-Phenyl-3-(4-(trifluoromethyl)phenyl)-1,2,4-oxadiazole (16). Yield 66% (193 mg), as a white solid: m.p = 91–93 °C (lit [129]. m.p = 91–92 °C); IR (KBr) ν_{max} (cm^{-1}): 3550, 3475, 3415, 3065, 2098, 1928, 1807, 1614, 1554, 1451, 1418, 1321, 1171, 1111, 918, 848, and 722; **^{1}H NMR{^{19}F}** (500 MHz, $CDCl_3$) δ_H: 8.23 (d, J = 10.5 Hz, 2H, Ar–**H**), 8.15 (d, J = 11 Hz, 2H, Ar–**H**), 7.70 (d, J = 10.0 Hz, 2H, Ar–**H**), 7.58–7.55 (m, 1H, Ar–**H**), 7.50 (t, J = 9 Hz, 2H, Ar–**H**); **^{13}C NMR{^{19}F}** (125 MHz, $CDCl_3$) δ_C: 176.2, 168.0 (oxadiazole-**C**), 132.9, 132.7, 130.3129.1, 128.1, 127.8 (Ar–**C**), 125.8 (**C**F$_3$), 123.9, 122.4 (Ar–**C**); EIMS m/z $[M]^+$ calcd for $[C_{15}H_9F_3N_2O]^+$: 290.06, found 290.03; Anal. Calcd for $C_{15}H_9F_3N_2O$: C, 62.07; H, 3.13; N, 9.65. Found: C, 62.40; H, 3.28; N, 9.53.

5.1.2.10. 5-(Pyridin-2-yl)-3-(4-(trifluoromethyl)phenyl)-1,2,4-oxadiazole (17). Yield 55% (160 mg), as a white solid: m.p = 109–111 °C; **^{1}H NMR** (500 MHz, DMSO-d_6) δ_H: 8.85 (dd, J = 4.5 Hz, 1.5 Hz, 1H, Py -**H**), 8.34 (d, J = 8 Hz, 1H, Py -**H**), 8.32 (dd, J = 8 Hz, 2 Hz, 2H, Ar–**H**), 8.13 (td, J = 7.5 Hz, 1.5 Hz, 1H, Py -**H**), 7.99 (d, J = 9 Hz, 2H, Ar–**H**), 7.74 (m, 1H, Py-**H**); **^{13}C NMR** (125 MHz, DMSO-d_6) δ_C: 174.8, 167.4 (oxadiazole-**C**), 150.6, 142.5, 138.2, 131.6 (q, $^2J_{CF}$ = 32.1 Hz, **C**-CF$_3$), 129.9, 128.0, 127.7, 126.37, 126.34 (Ar–**C,** Py -**C**), 124.6 (q, $^1J_{CF}$ = 271 Hz, **C**F$_3$); EIMS m/z $[M]^+$ calcd for $[C_{14}H_8F_3N_3O]^+$: 291.06, found 291.22; Anal. Calcd for $C_{14}H_8F_3N_3O$: C, 57.74; H, 2.77; N, 14.43. Found: C, 57.41; H, 2.91; N, 14.27.

5.1.2.11. 5-(Pyridin-4-yl)-3-(4-(trifluoromethyl)phenyl)-1,2,4-oxadiazole (18). Yield 59% (174 mg), as a white solid: m.p = 119–120 °C; IR (KBr) ν_{max} (cm^{-1}): 3381, 3057, 2101, 1936, 1807, 1654, 1577, 1322, 1142, 1542, 1417, 1059, 1018, 848, and 766; **^{1}H NMR** (500 MHz, DMSO-d_6) δ_H: 8.89 (dd, J = 5 Hz, 2 Hz, 2H, Py -**H**), 8.28 (d, J = 6.5 Hz 2H, Ar–**H**), 8.08 (dd, J = 4.5 Hz, 1.5 Hz, 2H, Py -**H**) 7.96 (d, J = 8 Hz 2H, Ar–**H**); **^{13}C NMR** (125 MHz, DMSO-d_6) δ_C: 174.4, 167.6 (oxadiazole-**C**), 151.3 (Py -**C**), 131.8 (q, $^2J_{CF}$ = 32.2 Hz, **C**-CF$_3$) 130.2, 129.6, 128.1, 126.44, 126.41,124.9 (Ar–**C,** Py -**C**), (q, $^1J_{CF}$ = 271 Hz, **C**F$_3$), 121.4 (Ar–**C**); EIMS m/z $[M]^+$ calcd for $[C_{14}H_8F_3N_3O]^+$: 291.06, found 291.47; Anal. Calcd for $C_{14}H_8F_3N_3O$: C, 57.74; H, 2.77; N, 14.43. Found: C, 57.38; H, 2.93; N, 14.22.

5.1.2.12. 2-(3-(4-(Trifluoromethyl)phenyl)-1,2,4-oxadiazol-5-yl) phenol (19). Yield 61% (185 mg), as a white solid: m.p = 162–163 °C; IR (KBr) ν_{max} (cm^{-1}): 3415, 3196, 1930, 2863, 1810, 1628, 1419, 1369, 1322, 1548, 1485, 1064, and 754; **^{1}H NMR {^{19}F}** (400 MHz, DMSO-d_6) δ_H: 10.70 (s, 1H, OH exchangeable with D_2O), 8.32 ((d, J = 10 Hz, 2H, Ar–**H**),8.03 (d, J = 8 Hz, 1H, Ar–**H**) 7.98 (d, J = 10.5 Hz, 2H, Ar–**H**), 7.56 (t, J = 10.5 Hz, 1H, Ar–**H**), 7.15 (d, J = 10.5 Hz, 1H, Ar–**H**), 7.06 (t, J = 9.5 Hz, 1H, Ar–**H**; **^{13}C NMR{^{19}F}** (100 MHz, DMSO-d_6) δ_C: 176.0, 166.8 (oxadiazole-**C**), 157.7, 135.4, 132.2, 131.7, 130.7, 130.5, 128.5 (Ar–**C**), 126.7 (**C**F$_3$), 120.2, 117.9, 110.22 (Ar–**C**); EIMS m/z $[M]^+$ calcd for $[C_{15}H_9F_3N_2O_2]^+$: 306.06, found 306.85; Anal. Calcd for $C_{15}H_9F_3N_2O_2$: C, 58.83; H, 2.96; N, 9.15. Found: C, 58.61; H, 3.14; N, 9.29.

5.1.2.13. 5-Methyl-3-(4-(trifluoromethyl)phenyl)-1,2,4-oxadiazole (20). Yield 72% (164 mg), as a White solid: m.p = 88–90 °C (lit [81]. m.p. 89–90 °C); **^{1}H NMR{^{19}F}** (400 MHz, $CDCl_3$) δ_H: 8.12 (d, J = 10 Hz, 2H, Ar–**H**), 7.67 (d, J = 10 Hz, 2H, Ar–**H**), 2.60 (s, 3H, C**H**$_3$); **^{13}C NMR{^{19}F}** (100 MHz, $CDCl_3$) δ_C: 177.0, 167.6 (oxadiazole-**C**), 133.1, 130.3, 127.7 (Ar–**C**), 125.9 (**C**F$_3$), 122.5 (Ar–**C**), 12.2 (C**H**$_3$); EIMS m/z $[M]^+$ calcd for $[C_{10}H_7F_3N_2O]^+$: 228.05, found 228.59; Anal. Calcd for $C_{10}H_7F_3N_2O$: C, 52.64; H, 3.09; N, 12.28. Found: C, 52.90; H, 3.31; N,

12.44.

5.1.2.14. 3-Methyl-5-phenyl-1,2,4-oxadiazole (21). Yield 79% (126 mg), as a white solid: m.p = 58–60 °C (lit [132]. m.p. 59–61 °C); IR (KBr) ν_{max} (cm^{-1}): 3549, 3475, 3415, 3060, 2925, 2853, 2086, 1824, 1778, 1615, 1561, 1480, 1338, 1273 and 786; **^{1}H NMR** (400 MHz, DMSO-d_6) δ_H: 8.08 (d, J = 6.5 Hz, 2H, Ar–**H**), 7.69 (t, J = 7.5 Hz, 1H, Ar–**H**), 7.61 (t, J = 8 Hz, 2H, Ar–**H**), 2.40 (s, 3H, C**H**$_3$); **^{13}C NMR** (100 MHz DMSO-d_6) δ_C: 174.6, 167.6 (oxadiazole-**C**), 133.1, 129.5, 127.7 (Ar–**C**), 123.4 (Ar–**C**), 11.2 (C**H**$_3$); EIMS m/z $[M]^+$ calcd for $[C_9H_8N_2O]^+$: 160.06, found 160.85; Anal. Calcd for $C_9H_8N_2O$: C, 67.49; H, 5.03; N, 17.49. Found: C, 67.80; H, 5.34; N, 17.21.

5.2. Biological evaluation

5.2.1. In vitro antioxidant activity

5.2.1.1. Free radical scavenging activity by the 1,1-Diphenyl-2-picrylhydrazyl (DPPH). Free radical scavenging activities of all the synthesized 1,2,4-oxadiazole derivatives **8**–**21** were assayed utilizing 1,1-Diphenyl-2-picrylhydrazyl (DPPH) as reported [85]. All samples were incubated with DPPH (0.004% in methanol) for 30 min in the dark. Then, the sample absorbance was measured at λ = 517 nm. The percentage of the free radical scavenging at the corresponding Log concentration of each sample was used for calculating the IC_{50} value (50% inhibitory concentration) using the GraphPad Instat software.

5.2.1.2. Iron chelating activity. Fe^{2+} chelating activities of the studied 1,2,4-oxadiazole derivatives **8**–**21** were determined by measuring the decrease in the Fe^{2+}-phenanthroline complex formation as reported [86]. Serial concentrations of the tested derivatives were mixed with Tris buffer (84 μl of 0.1 M, pH 7.4), saline (109 μl), and $FeSO_4$ (1 mM). After 10 min, 1,10 phenanthroline (10 μl) was added. EDTA was utilized as a positive control. The generated red colored complex was measured using a microplate reader (BMG LabTech, Germany) at λ = 510 nm for estimating the percentage of iron chelating activity. The effective concentration (EC_{50}) values (at 50% iron chelation) of the evaluated 1,2,4-oxadiazoles were calculated by the Graphpad Instat software.

5.2.2. Cytotoxicity screening on normal human cells

Normal lung fibroblasts (Wi-38) cells were cultured in DMEM medium-contained 10% fetal bovine serum (FBS), seeded as 5×10^3 cells per well in a 96-well cell culture plate, then incubated at 37 °C in a 5% CO_2 incubator. After 24 h. for cell attachment, serial concentrations of all the synthesized 1,2,4-oxadiazoles **8**–**21** and the reference chemotherapy (doxorubicin) were incubated with Wi-38 cells for 72 h. then the cell viability was assayed by MTT method [71–73], where twenty 20 μL of 5 mg/ml MTT (Sigma, USA) was added to each well and the plate was incubated at 37 °C for 3 h. Then, MTT solution was removed, 100 μl DMSO was added, and the absorbance of each well was measured with a microplate reader (BMG LabTech, Germany) at λ = 570 nm. The effective safe concentration (EC_{100}) value (at 100% cell viability) and the half-maximal inhibitory concentration (IC_{50}) value (at 50% cell viability) of the tested compounds were estimated by the Graphpad Instat software.

5.2.3. Anticancer evaluation

The studied 1,2,4-oxadiazoles were evaluated for their anticancer potential, in comparison with doxorubicin against HepG-2, MDA-MB231, and Caco-2 cells. HepG-2 and MDA-MB231 were cultured in RPMI-1640 (Lonza, USA) supplemented with 10% FBS, while Caco-2 cells were cultured in DMEM (Lonza, USA) contained with 10% FBS. All cancer cells (4×10^3 cells/well) were seeded in sterile 96-well plates. After 24 h, serial concentrations of the tested compounds were incubated with the three cancer cell lines for 72 h. at 37 °C in a 5% CO_2 incubator. MTT method [71–73] was performed as described above. IC_{50} values of the studied compounds were calculated using the Graphpad Instat software. Furthermore, cellular morphological changes before and after treatment with the most active and safest anticancer derivatives **11, 15,** and **19** were investigated using a phase-contrast inverted microscope with a digital camera (Olympus, Japan).

5.2.4. Flow cytometric analysis of apoptosis

IC_{50} doses of the selected promising derivatives **11, 15,** and **19** were incubated for 72 h with HepG-2, MDA-MB231, and Caco-2 cells. After trypsinization, the untreated and treated cells were incubated with annexin V/PI for 15 min. Then, cells were fixed and incubated with streptavidin-fluorescein (5 μg/mL) for 15 min. The apoptosis-dependent anticancer effect was determined by quantification of annexin-stained apoptotic cells using the FITC signal detector (FL1) against the phycoerythrin emission signal detector (FL2).

5.2.5. Intracellular ROS scavenging activity

The intracellular ROS level was quantified by incubation of the untreated and treated HepG-2 cells with 5 μM of 2,7-dichlorodihydrofluorescin diacetate ($DCFH_2$-DA) [133] for 30 min at 37 °C in the dark. Then, cells were trypsinized and suspended in phosphate buffer saline. The intensity of the fluorescence was analyzed by a flow cytometer with excitation and emission wavelengths at 488 nm and 530 nm, respectively.

5.2.6. Nrf2 activation

A high throughput assay combining a quick ELISA format with a specific and sensitive non-radioactive assay was employed utilizing Nrf2 Transcription Factor Assay Kit (ab207223) for transcription factor activation in HepG-2 cells. Herein, a double-stranded DNA sequence with Nrf2 consensus binding site (5′–GTCACAGTGACTCAGCAGAATCTG–3′) was immobilized on a 96-well plate. The specified sample concentration (EC_{100} dose on normal cells), positive control, and blank were added to the relevant wells. The nuclear extract active Nrf2 binds specifically to the oligonucleotide and is detected by a primary antibody that can recognize a specific epitope of Nrf2 that is only accessible when the protein is activated and bound to the target DNA. An HRP-conjugated secondary antibody provides sensitive colorimetric readout at OD 450 nm. The detailed procedures are described in the **supplementary data**.

5.2.7. Thioredoxin reductase inhibition

In vitro TrxR inhibitory activities of the studied compounds were evaluated utilizing Thioredoxin Reductase Colorimetric Assay Kit - Cayman chemical (Cat # 10007892). The assay is based on the reduction of 5,5′-dithio-bis(2-dinitrobenzoicacid (DTNB) to 5-thio-2-nitrobenzoic acid (TNB) with NADPH producing a yellow product that can be measured at 405–414 nm. The procedure and data analysis are detailed in the **supplementary data**.

5.2.8. In vitro IKKα inhibition

The studied compounds were evaluated for *in vitro* IKKα inhibitory activities utilizing IKKα kinase Assay-Promega Corporation Kit comprising ADP-Glo™ Kinase Assay (Cat #V9101) and IKKα Kinase Enzyme System (Cat #V4068). It is a luminescent kinase assay that detects ADP resulted from kinase reaction. Then, ADP is converted to ATP that is converted into light by Ultra-GloTM Luciferase. The luminescent signal correlates with kinase activity and ADP amount. The procedure and data analysis were carried out

as described in the **supplementary data.**

5.2.9. Quantitative real-time PCR analysis of NF-κB

RNAs of untreated and the tested compounds-treated HepG-2 cells were extracted using Gene JET RNA Purification Kit (Thermo Scientific, USA). The cDNA was synthesized from mRNA using cDNA Synthesis Kit (Thermo Scientific, USA). Real-time PCR was performed using SYBR green master mix and specific primers (Forward/Reverse) were 5′-TACTCTGGCGCAGAAATTAGGTC-3′/5′-CTGTCTCGGAGCTCGTCTATTTG-3′ for NF-kappa B gene. The $2^{-\Delta\Delta CT}$ equation was used to estimate the change in gene expressions of NF-kB.

5.2.10. In vitro NADPH oxidase inhibition

Compounds were tested for NADPH oxidase inhibitory activities utilizing Human NADPH Oxidase 4 (NOX4) ELISA Kit (Cat # MBS901457). The assay employs the quantitative sandwich enzyme immunoassay technique, where a specific NOX antibody was pre-coated onto a microplate. Then, samples were pipetted in the specified wells. Any existing NOX remained bound by its immobilized antibody. After washing unbound substances, a biotin-conjugated NOX4 specific antibody was added to the wells, followed by avidin-conjugated Horseradish Peroxidase (HRP). A substrate solution was added to the wells after a wash. The color was then detected in proportion to the initially bound NOX. The detailed procedure and data analysis are mentioned in the **supplementary data**.

5.3. Molecular modeling studies

5.3.1. Docking

Docking simulations were performed employing Molecular Operating Environment (MOE) software package version 2015.10 [103], Chemical Computing Group, Montreal, Canada. The enzymes crystal structures were obtained from the protein data bank. Docking parameters were validated by first re-docking of the co-crystallized ligand or the reported inhibitor with RMSD value < 2 Å whenever applicable. The 'Site Finder' feature was employed to seek the binding site pockets considering the reported key amino acids whenever needed. Energy minimization and geometry optimization of the studied oxadiazoles were done through the MOE dock tool prior to docking. The ligand placement method was set to apply the Triangular matcher algorithm. Alpha HB scoring function was employed as the default scoring function generating the top 5 non-redundant poses of the lowest binding energy conformers of the test ligands.

5.3.2. In silico prediction of physicochemical properties, ADMET and drug-likeness parameters

Physicochemical properties and drug-likeness were computed by *SwissADME* [119] and *MolSoft* [66] software. ADME profiling was performed by PreADMET calculator [91]. Toxicity was predicted by PROTOX [123].

5.4. Data analysis and statistics

Data were expressed as mean ± standard error of the mean (SEM). Statistical significance was estimated by the multiple comparisons Tukey post-hoc analysis of variance (ANOVA) using the SPSS16 program. The differences were considered statistically significant at $p < 0.05$ and expressed by different letters i.e., different letters (a, b, c, and d) are significantly different at $P < 0.05$.

Declaration of competing interest

The authors declare that they have no known competing financial interests or personal relationships that could have appeared to influence the work reported in this paper.

Appendix A. Supplementary data

Supplementary data to this article can be found online at https://doi.org/10.1016/j.ejmech.2021.113475.

References

[1] D. Hanahan, Robert A. Weinberg, Hallmarks of cancer: the next generation, Cell 144 (2011) 646–674.
[2] M.B. Azad, Y. Chen, S.B. Gibson, Regulation of autophagy by reactive oxygen species (ROS): implications for cancer progression and treatment, Antioxidants Redox Signal. 11 (2008) 777–790.
[3] G.-Y. Liou, P. Storz, Reactive oxygen species in cancer, Free Radic. Res. 44 (2010) 479–496.
[4] V. Sosa, T. Moliné, R. Somoza, R. Paciucci, H. Kondoh, M.E. Lleonart, Oxidative stress and cancer: an overview, Ageing Res. Rev. 12 (2013) 376–390.
[5] A.M. Sashi Papu John, M.K. Ankem, C. Damodaran, Oxidative stress: a promising target for chemoprevention, Curr. Pharmacol. Rep. 2 (2016) 73–81.
[6] D. Thapa, R. Ghosh, Antioxidants for prostate cancer chemoprevention: challenges and opportunities, Biochem. Pharmacol. 83 (2012) 1319–1330.
[7] M. Monireh, S. Farhad, M.F. Mohammad, K. Majid, Anti-oxidants as chemo-preventive agents in prostate cancer: a gap between preclinical and clinical studies, Recent Pat. Anti-Cancer Drug Discov. 13 (2018) 224–239.
[8] L.W. Wattenberg, Chemoprevention of cancer, Canc. Res. 45 (1985) 1–8.
[9] S. Piccolella, S. Pacifico, Plant-derived polyphenols: a chemopreventive and chemoprotectant worth-exploring resource in toxicology, in: Advances in Molecular Toxicology, Elsevier, 2015, pp. 161–214.
[10] M.C. Jaramillo, D.D. Zhang, The emerging role of the Nrf2–Keap1 signaling pathway in cancer, Genes Dev. 27 (2013) 2179–2191.
[11] M. Battino, F. Giampieri, F. Pistollato, A. Sureda, M.R. de Oliveira, V. Pittalà, F. Fallarino, S.F. Nabavi, A.G. Atanasov, S.M. Nabavi, Nrf2 as regulator of innate immunity: a molecular Swiss army knife!, Biotechnol. Adv. 36 (2018) 358–370.
[12] B.M. Hybertson, B. Gao, S.K. Bose, J.M. McCord, Oxidative stress in health and disease: the therapeutic potential of Nrf2 activation, Mol. Aspect. Med. 32 (2011) 234–246.
[13] S. Kovac, P.R. Angelova, K.M. Holmström, Y. Zhang, A.T. Dinkova-Kostova, A.Y. Abramov, Nrf2 regulates ROS production by mitochondria and NADPH oxidase, Biochim. Biophys. Acta 1850 (2015) 794–801.
[14] W. Dröge, Free radicals in the physiological control of cell function, Physiol. Rev. 82 (2002) 47–95.
[15] S. Vomund, A. Schäfer, M.J. Parnham, B. Brüne, A. Von Knethen, Nrf2, the master regulator of anti-oxidative responses, Int. J. Mol. Sci. 18 (2017).
[16] E. Panieri, A. Buha, P. Telkoparan-Akillilar, D. Cevik, D. Kouretas, A. Veskoukis, Z. Skaperda, A. Tsatsakis, D. Wallace, S. Suzen, L. Saso, Potential applications of NRF2 modulators in cancer therapy, Antioxidants 9 (2020).
[17] X. Yu, T. Kensler, Nrf2 as a target for cancer chemoprevention, Mutat Res-Fund Mol M 591 (2005) 93–102.
[18] H. Zhou, Y. Wang, Q. You, Z. Jiang, Recent progress in the development of small molecule Nrf2 activators: a patent review (2017-present), Expert Opin. Ther. Pat. 30 (2020) 209–225.
[19] H. Sun, J. Zhu, H. Lin, K. Gu, F. Feng, Recent progress in the development of small molecule Nrf2 modulators: a patent review (2012-2016), Expert Opin. Ther. Pat. 27 (2017) 763–785.
[20] S. Crunkhorn, Abbott boosts investment in NRF2 activators for reducing oxidative stress, Nat. Rev. Drug Discov. 11 (2012), 96-96.
[21] N. Robledinos-Antón, R. Fernández-Ginés, G. Manda, A. Cuadrado, Activators and inhibitors of NRF2: a review of their potential for clinical development, Oxid. Med. Cell. Longev. (2019) 2019, 9372182.
[22] Q. Wang, S. Chuikov, S. Taitano, Q. Wu, A. Rastogi, S.J. Tuck, J.M. Corey, S.K. Lundy, Y. Mao-Draayer, Dimethyl fumarate protects neural stem/progenitor cells and neurons from oxidative damage through nrf2-ERK1/2 MAPK pathway, Int. J. Mol. Sci. 16 (2015) 13885–13907.
[23] J. Callahan, J. Kerns, P. Li, T. Li, B. McCleland, H. Nie, J. Pero, T. Davies, M. Grazia Carr, C. Griffiths-Jones, Biaryl Pyrazoles as Nrf2 Regulators, WO2017/60854, 2017.
[24] J. Callahan, J. Kerns, T. Li, H. Nie, J. Pero, T. Davies, T. Heightman, A. Woolford, C. Griffiths-Jones, D. Norton, Arylcyclohexyl Pyrazoles as NRF2 Regulators, WO2017060855, 2017.
[25] A.D. Jain, H. Potteti, B.G. Richardson, L. Kingsley, J.P. Luciano, A.F. Ryuzoji, H. Lee, A. Krunic, A.D. Mesecar, S.P. Reddy, T.W. Moore, Probing the structural requirements of non-electrophilic naphthalene-based Nrf2 activators, Eur. J. Med. Chem. 103 (2015) 252–268.
[26] D.D. Zhang, Bardoxolone brings nrf2-based therapies to light, Antioxidants

Redox Signal. 19 (2012) 517–518.
[27] L.-L. Xu, Y.-F. Wu, L. Wang, C.-C. Li, L. Li, B. Di, Q.-D. You, Z.-Y. Jiang, Structure-activity and structure-property relationships of novel Nrf2 activators with a 1,2,4-oxadiazole core and their therapeutic effects on acetaminophen (APAP)-induced acute liver injury, Eur. J. Med. Chem. 157 (2018) 1376–1394.
[28] L.-L. Xu, J.-F. Zhu, X.-L. Xu, J. Zhu, L. Li, M.-Y. Xi, Z.-Y. Jiang, M.-Y. Zhang, F. Liu, M.-c. Lu, Q.-C. Bao, Q. Li, C. Zhang, J.-L. Wei, X.-J. Zhang, L.-S. Zhang, Q.-D. You, H.-P. Sun, Discovery and modification of in vivo active Nrf2 activators with 1,2,4-oxadiazole core: hits identification and structure–activity relationship study, J. Med. Chem. 58 (2015) 5419–5436.
[29] L.-L. Xu, X. Zhang, Z.-Y. Jiang, Q.-D. You, Molecular similarity guided optimization of novel Nrf2 activators with 1,2,4-oxadiazole core, Bioorg. Med. Chem. 24 (2016) 3540–3547.
[30] L.-L. Xu, T. Liu, L. Wang, L. Li, Y.-F. Wu, C.-C. Li, B. Di, Q.-D. You, Z.-Y. Jiang, 3-(1H-Benzo [d] imidazole-6-yl)-5-(4-fluorophenyl)-1,2,4-oxadiazole (DDO7232), a novel potent Nrf2/ARE inducer, ameliorates DSS-induced murine colitis and protects NCM460 cells against oxidative stress via ERK1/2 phosphorylation, Oxid. Med. Cell. Longev. 2018 (2018) 3271617.
[31] L.-L. Xu, Y.-F. Wu, F. Yan, C.-C. Li, Z. Dai, Q.-D. You, Z.-Y. Jiang, B. Di, 5-(3,4-Difluorophenyl)-3-(6-methylpyridin-3-yl)-1,2,4-oxadiazole (DDO-7263), a novel Nrf2 activator targeting brain tissue, protects against MPTP-induced subacute Parkinson's disease in mice by inhibiting the NLRP3 inflammasome and protects PC12 cells against oxidative stress, Free Radic. Biol. Med. 134 (2019) 288–303.
[32] K. Kavitha, P. Thiyagarajan, J. Rathna @ Nandhini, R. Mishra, S. Nagini, Chemopreventive effects of diverse dietary phytochemicals against DMBA-induced hamster buccal pouch carcinogenesis via the induction of Nrf2-mediated cytoprotective antioxidant, detoxification, and DNA repair enzymes, Biochimie 95 (2013) 1629–1639.
[33] A. Kobayashi, M.-I. Kang, H. Okawa, M. Ohtsuji, Y. Zenke, T. Chiba, K. Igarashi, M. Yamamoto, Oxidative stress sensor Keap1 functions as an adaptor for cul3-based E3 ligase to regulate proteasomal degradation of Nrf2, Mol. Cell Biol. 24 (2004) 7130.
[34] M. Kobayashi, L. Li, N. Iwamoto, Y. Nakajima-Takagi, H. Kaneko, Y. Nakayama, M. Eguchi, Y. Wada, Y. Kumagai, M. Yamamoto, The antioxidant defense system keap1-nrf2 comprises a multiple sensing mechanism for responding to a wide range of chemical compounds, Mol. Cell Biol. 29 (2009) 493.
[35] T. Nguyen, P.J. Sherratt, H.C. Huang, C.S. Yang, C.B. Pickett, Increased protein stability as a mechanism that enhances nrf2-mediated transcriptional activation of the antioxidant response element: DEGRADATION OF Nrf2 BY the 26 S proteasome, J. Biol. Chem. 278 (2003) 4536–4541.
[36] C. Zhuang, Z. Wu, C. Xing, Z. Miao, Small molecules inhibiting Keap1–Nrf2 protein–protein interactions: a novel approach to activate Nrf2 function, MedChemComm 8 (2017) 286–294.
[37] D. Mustacich, G. Powis, Thioredoxin reductase, Biochem. J. 346 (2000) 1–8.
[38] M. Luthman, A. Holmgren, Rat liver thioredoxin and thioredoxin reductase: purification and characterization, Biochemistry 21 (1982) 6628–6633.
[39] S.V. Iverson, S. Eriksson, J. Xu, J.R. Prigge, E.A. Talago, T.A. Meade, E.S. Meade, M.R. Capecchi, E.S.J. Arnér, E.E. Schmidt, A Txnrd1-dependent metabolic switch alters hepatic lipogenesis, glycogen storage, and detoxification, Free Radic. Biol. Med. 63 (2013) 369–380.
[40] X. Peng, P.K. Mandal, V.O. Kaminskyy, A. Lindqvist, M. Conrad, E.S.J. Arnér, Sec-containing TrxR1 is essential for self-sufficiency of cells by control of glucose-derived H2O2, Cell Death Dis. 5 (2014) e1235-e1235.
[41] J.R. Prigge, S. Eriksson, S.V. Iverson, T.A. Meade, M.R. Capecchi, E.S.J. Arnér, E.E. Schmidt, Hepatocyte DNA replication in growing liver requires either glutathione or a single allele of txnrd1, Free Radic. Biol. Med. 52 (2012) 803–810.
[42] E.S. Suvorova, O. Lucas, C.M. Weisend, M.F. Rollins, G.F. Merrill, M.R. Capecchi, E.E. Schmidt, Cytoprotective Nrf2 pathway is induced in chronically txnrd 1-deficient hepatocytes, PloS One 4 (2009) e6158.
[43] M. Cebula, E.E. Schmidt, E.S.J. Arnér, TrxR1 as a potent regulator of the nrf2-keap1 response system, Antioxidants Redox Signal. 23 (2015) 823–853.
[44] W. Cai, L. Zhang, Y. Song, B. Wang, B. Zhang, X. Cui, G. Hu, Y. Liu, J. Wu, J. Fang, Small molecule inhibitors of mammalian thioredoxin reductase, Free Radic. Biol. Med. 52 (2012) 257–265.
[45] E.-H. Chew, A.A. Nagle, Y. Zhang, S. Scarmagnani, P. Palaniappan, T.D. Bradshaw, A. Holmgren, A.D. Westwell, Cinnamaldehydes inhibit thioredoxin reductase and induce Nrf2: potential candidates for cancer therapy and chemoprevention, Free Radic. Biol. Med. 48 (2010) 98–111.
[46] K.K. Kaminska, H.C. Bertrand, H. Tajima, W.C. Stafford, Q. Cheng, W. Chen, G. Wells, E.S.J. Arner, E.-H. Chew, Indolin-2-one compounds targeting thioredoxin reductase as potential anticancer drug leads, Oncotarget 7 (2016) 40233.
[47] F.-F. Gan, K.K. Kaminska, H. Yang, C.-Y. Liew, P.-C. Leow, C.-L. So, L.N.L. Tu, A. Roy, C.-W. Yap, T.-S. Kang, W.-K. Chui, E.-H. Chew, Identification of michael acceptor-centric pharmacophores with substituents that yield strong thioredoxin reductase inhibitory character correlated to anti-proliferative activity, Antioxidants Redox Signal. 19 (2013) 1149–1165.
[48] S.M.U. Ahmed, L. Luo, A. Namani, X.J. Wang, X. Tang, Nrf2 signaling pathway: pivotal roles in inflammation, Biochim. Biophys. Acta (BBA) - Mol. Basis Dis. 1863 (2017) 585–597.
[49] N. Khurana, S.C. Sikka, Targeting crosstalk between nrf-2, NF-κB and androgen receptor signaling in prostate cancer, Cancers 10 (2018) 352.
[50] G.-H. Liu, J. Qu, X. Shen, NF-κB/p65 antagonizes Nrf2-ARE pathway by depriving CBP from Nrf2 and facilitating recruitment of HDAC3 to MafK, Biochim. Biophys. Acta Mol. Cell Res. 1783 (2008) 713–727.
[51] M. Yu, H. Li, Q. Liu, F. Liu, L. Tang, C. Li, Y. Yuan, Y. Zhan, W. Xu, W. Li, H. Chen, C. Ge, J. Wang, X. Yang, Nuclear factor p65 interacts with Keap1 to repress the Nrf2-ARE pathway, Cell. Signal. 23 (2011) 883–892.
[52] K.M. Oliver, J.F. Garvey, C.T. Ng, D.J. Veale, U. Fearon, E.P. Cummins, C.T. Taylor, Hypoxia activates NF-κB–Dependent gene expression through the canonical signaling pathway, Antioxidants Redox Signal. 11 (2009) 2057–2064.
[53] G. Gloire, J. Piette, Redox regulation of nuclear post-translational modifications during NF-κB activation, Antioxidants Redox Signal. 11 (2009) 2209–2222.
[54] C. Gamble, K. McIntosh, R. Scott, K.H. Ho, R. Plevin, A. Paul, Inhibitory kappa B kinases as targets for pharmacological regulation, Br. J. Pharmacol. 165 (2012) 802–819.
[55] K. Undheim, Five-membered Rings (One Oxygen or Sulfur and at Least One Nitrogen Atom) Fused with Six-Membered Rings (At Least One Nitrogen Atom), 1984.
[56] S. Urig, K. Becker, On the potential of thioredoxin reductase inhibitors for cancer therapy, Semin. Canc. Biol. 16 (2006) 452–465.
[57] G.A. Patani, E.J. LaVoie, Bioisosterism: A rational approach in drug design, Chem. Rev. 96 (1996) 3147–3176.
[58] J. Boström, A. Hogner, A. Llinàs, E. Wellner, A.T. Plowright, Oxadiazoles in medicinal chemistry, J. Med. Chem. 55 (2012) 1817–1830.
[59] H. Ogawa, M. Azuma, S. Muto, Y. Nishioka, A. Honjo, T. Tezuka, H. Uehara, K. Izumi, A. Itai, S. Sone, IκB kinase β inhibitor IMD-0354 suppresses airway remodelling in a Dermatophagoides pteronyssinus-sensitized mouse model of chronic asthma, Clin. Exp. Allergy 41 (2011) 104–115.
[60] A. Sugita, H. Ogawa, M. Azuma, S. Muto, A. Honjo, H. Yanagawa, Y. Nishioka, K. Tani, A. Itai, S. Sone, Antiallergic and anti-inflammatory effects of a novel IκB kinase β inhibitor, IMD-0354, in a mouse model of allergic inflammation, Int. Arch. Allergy Immunol. 148 (2009) 186–198.
[61] A. Tanaka, M. Konno, S. Muto, N. Kambe, E. Morii, T. Nakahata, A. Itai, H. Matsuda, A novel NF-κB inhibitor, IMD-0354, suppresses neoplastic proliferation of human mast cells with constitutively activated c-kit receptors, Blood 105 (2005) 2324–2331.
[62] C.D. Mohan, N.C. Anilkumar, S. Rangappa, M.K. Shanmugam, S. Mishra, A. Chinnathambi, S.A. Alharbi, A. Bhattacharjee, G. Sethi, A.P. Kumar, Basappa, K.S. Rangappa, Novel 1,3,4-oxadiazole induces anticancer activity by targeting NF-κB in hepatocellular carcinoma cells, Front. Oncol. 8 (2018) 42.
[63] M.S.S. Palanki, P.E. Erdman, A.M. Manning, A. Ow, L.J. Ransone, C. Spooner, C. Suto, M. Suto, Novel inhibitors of AP-1 and NF-κB mediated gene expression: structure–activity relationship studies of ethyl 4-[(3-Methyl-2,5-dioxo(3-pyrrolinyl))amino]-2-(trifluoromethyl)pyrimidine-5-carboxylate, Bioorg. Med. Chem. Lett 10 (2000) 1645–1648.
[64] M. Gobec, T. Tomašič, T. Markovič, I. Mlinarič-Raščan, M.S. Dolenc, Ž. Jakopin, Antioxidant and anti-inflammatory properties of 1,2,4-oxadiazole analogs of resveratrol, Chem. Biol. Interact. 240 (2015) 200–207.
[65] Y.-Y. Zhang, Q.-Q. Zhang, J. Zhang, J.-L. Song, J.-C. Li, K. Han, J.-T. Huang, C.-S. Jiang, H. Zhang, Synthesis and evaluation of 1,2,4-oxadiazole derivatives as potential anti-inflammatory agents by inhibiting NF-κB signaling pathway in LPS-stimulated RAW 264.7 cells, Bioorg. Med. Chem. Lett 30 (2020) 127373.
[66] J.P. Adjimani, P. Asare, Antioxidant and free radical scavenging activity of iron chelators, Toxicol. Rep. 2 (2015) 721–728.
[67] M.U. Imam, S. Zhang, J. Ma, H. Wang, F. Wang, Antioxidants mediate both iron homeostasis and oxidative stress, Nutrients 9 (2017) 1–19.
[68] S. Xiong, H. She, H. Takeuchi, B. Han, J.F. Engelhardt, C.H. Barton, E. Zandi, C. Giulivi, H. Tsukamoto, Signaling role of intracellular iron in NF-κB activation, J. Biol. Chem. 278 (2003) 17646–17654.
[69] W.-H. Liu, Y.-J. Chen, J.-H. Chien, L.-S. Chang, Amsacrine suppresses matrix metalloproteinase-2 (MMP-2)/MMP-9 expression in human leukemia cells, J. Cell. Physiol. 229 (2014) 588–598.
[70] J. Ferlay, M. Colombet, I. Soerjomataram, C. Mathers, D.M. Parkin, M. Piñeros, A. Znaor, F. Bray, Estimating the global cancer incidence and mortality in 2018: GLOBOCAN sources and methods, Int. J. Canc. 144 (2019) 1941–1953.
[71] M.S. Ayoup, M.A. Fouad, H. Abdel-Hamid, E.S. Ramadan, M.M. Abu-Serie, A. Noby, M. Teleb, Battle tactics against MMP-9; discovery of novel non-hydroxamate MMP-9 inhibitors endowed with PI3K/AKT signaling attenuation and caspase 3/7 activation via Ugi bis-amide synthesis, Eur. J. Med. Chem. 186 (2020) 111875.
[72] T. Mosmann, Rapid colorimetric assay for cellular growth and survival: application to proliferation and cytotoxicity assays, J. Immunol. Methods 65 (1983) 55–63.
[73] M. Salah Ayoup, Y. Wahby, H. Abdel-Hamid, E.S. Ramadan, M. Teleb, M.M. Abu-Serie, A. Noby, Design, synthesis and biological evaluation of novel α-acyloxy carboxamides via Passerini reaction as caspase 3/7 activators, Eur. J. Med. Chem. 168 (2019) 340–356.
[74] H. Chen, O. Engkvist, T. Kogej, Chapter 15 - compound properties and their influence on drug quality, in: C.G. Wermuth, D. Aldous, P. Raboisson, D. Rognan (Eds.), The Practice of Medicinal Chemistry, fourth ed., Academic Press, San Diego, 2015, pp. 379–393.
[75] C.H. Reynolds, B.A. Tounge, S.D. Bembenek, Ligand binding efficiency: trends, physical basis, and implications, J. Med. Chem. 51 (2008) 2432–2438.
[76] G.M. Keserü, G.M. Makara, The influence of lead discovery strategies on the

properties of drug candidates, Nat. Rev. Drug Discov. 8 (2009) 203–212.
[77] J.A. Arnott, R. Kumar, S.L. Planey, Lipophilicity indices for drug development, J Appl. Biopharm. Pharmacokinet 1 (2013) 31–36.
[78] I. Jabeen, K. Pleban, U. Rinner, P. Chiba, G.F. Ecker, Structure–activity relationships, ligand efficiency, and lipophilic efficiency profiles of benzophenone-type inhibitors of the multidrug transporter P-glycoprotein, J. Med. Chem. 55 (2012) 3261–3273.
[79] T.T. Wager, R.Y. Chandrasekaran, X. Hou, M.D. Troutman, P.R. Verhoest, A. Villalobos, Y. Will, Defining desirable central nervous system drug space through the alignment of molecular properties, in vitro ADME, and safety attributes, ACS Chem. Neurosci. 1 (2010) 420–434.
[80] E.S.H. El Ashry, L.F. Awad, M. Teleb, N.A. Ibrahim, M.M. Abu-Serie, M.N. Abd Al Moaty, Structure-based design and optimization of pyrimidine- and 1,2,4-triazolo[4,3-a]pyrimidine-based matrix metalloproteinase-10/13 inhibitors via Dimroth rearrangement towards targeted polypharmacology, Bioorg. Chem. 96 (2020) 103616.
[81] S. Baykov, T. Sharonova, A. Shetnev, S. Rozhkov, S. Kalinin, A.V. Smirnov, The first one-pot ambient-temperature synthesis of 1,2,4-oxadiazoles from amidoximes and carboxylic acid esters, Tetrahedron 73 (2017) 945–951.
[82] A. Vörös, Z. Baán, P. Mizsey, Z. Finta, formation of aromatic amidoximes with hydroxylamine using microreactor technology, Org. Process Res. Dev. 16 (2012) 1717–1726.
[83] C.J. Pimentel Barros, J.J. Freitas, R.N. Oliveira, J.R. Freitas Filho, Synthesis of amidoximes using an efficient and rapid ultrasound method, J. Chil. Chem. Soc. 56 (2011) 721–722.
[84] F. Eloy, R. Lenaers, The chemistry of amidoximes and related compounds, Chem. Rev. 62 (1962) 155–183.
[85] A. Braca, N. De Tommasi, L. Di Bari, C. Pizza, M. Politi, I. Morelli, Antioxidant principles from Bauhinia tarapotensis, J. Nat. Prod. 64 (2001) 892–895.
[86] G. Minotti, S.D. Aust, An investigation into thee mechanism of citrate Fe^{2+} dependent lipid peroxidation, Free Radic. Biol. Med. 3 (1987) 379–387.
[87] I. Grigalius, V. Petrikaite, Relationship between antioxidant and anticancer activity of trihydroxyflavones, Molecules 22 (2017) 2169.
[88] K. Saravanakumar, R. Chelliah, X. Hu, D.-H. Oh, K. Kathiresan, M.-H. Wang, Antioxidant, anti-lung cancer, and anti-bacterial activities of toxicodendron vernicifluum, Biomolecules 9 (2019) 127.
[89] R.R. Khalil, Y.F. Mustafa, Phytochemical, antioxidant and antitumor studies of coumarins extracted from granny smith apple seeds by different methods, Sys. Rev. Pharm. 11 (2020) 57–63.
[90] B.S. Jayashree, M. Kaur, A. Pai, Synthesis, characterisation, antioxidant and anticancer evaluation of novel schiff's bases of 2-quinolones, Elixir Online Journal 52 (2012) 11317–11322.
[91] P. Prayong, S. Barusrux, N. Weerapreeyakul, Cytotoxic activity screening of some indigenous Thai plants, Fitoterapia 79 (2008) 598–601.
[92] O.H. Rizk, M. Teleb, M.M. Abu-Serie, O.G. Shaaban, Dual VEGFR-2/PIM-1 kinase inhibition towards surmounting the resistance to antiangiogenic agents via hybrid pyridine and thienopyridine-based scaffolds: design, synthesis and biological evaluation, Bioorg. Chem. 92 (2019) 103189.
[93] N. Cenas, S. Prast, H. Nivinskas, J. Sarlauskas, E.S.J. Arnér, Interactions of nitroaromatic compounds with the mammalian selenoprotein thioredoxin reductase and the relation to induction of apoptosis in human cancer cells*, J. Biol. Chem. 281 (2006) 5593–5603.
[94] K. Anestål, S. Prast-Nielsen, N. Cenas, E.S.J. Arnér, Cell death by SecTRAPs: thioredoxin reductase as a prooxidant killer of cells, PloS One 3 (2008), e1846.
[95] G.W. Peet, J. Li, IκB kinases α and β show a random sequential kinetic mechanism and are inhibited by staurosporine and quercetin, J. Biol. Chem. 274 (1999) 32655–32661.
[96] S. Wang, S. Kotamraju, E. Konorev, S. Kalivendi, J. Joseph, B. Kalyanaraman, Activation of nuclear factor-κB during doxorubicin-induced apoptosis in endothelial cells and myocytes is pro-apoptotic: the role of hydrogen peroxide, Biochem. J. 367 (2002) 729–740.
[97] R. Miesel, D. Sanocka, M. Kurpisz, H. Kröger, Antiinflammatory effects of nadph oxidase inhibitors, J. Inflamm. 19 (1995) 347–362.
[98] D.M. Pereira, P. Valentão, J.A. Pereira, P.B. Andrade, Phenolics: from chemistry to biology, Molecules 14 (2009) 2202–2211.
[99] C.S. Yang, J.M. Landau, M.-T. Huang, H.L. Newmark, Inhibition of carcinogenesis by dietary polyphenolic compounds, Annu. Rev. Nutr. 21 (2001) 381–406.
[100] G. Salassa, A. Terenzi, Metal complexes of oxadiazole ligands: an overview, Int. J. Mol. Sci. 20 (2019) 3483.
[101] P.C.H. Hollman, Evidence for health benefits of plant phenols: local or systemic effects? J. Sci. Food Agric. 81 (2001) 842–852.
[102] A. Basli, N. Belkacem, I. Amrani, Health Benefits of Phenolic Compounds against Cancers, Phenolic Compounds–Biological Activity, IntechOpen, London, UK, 2017, pp. 193–210.
[103] C.C.G. Molecular Operating Environment (MOE), Montreal, Canada, http://www.chemcomp.com.
[104] T. Sandalova, L. Zhong, Y. Lindqvist, A. Holmgren, G. Schneider, Three-dimensional structure of a mammalian thioredoxin reductase: implications for mechanism and evolution of a selenocysteine-dependent enzyme, Proc. Natl. Acad. Sci. Unit. States Am. 98 (2001) 9533.
[105] J. Nordberg, L. Zhong, A. Holmgren, E.S.J. Arnér, Mammalian thioredoxin reductase is irreversibly inhibited by dinitrohalobenzenes by alkylation of both the redox active selenocysteine and its neighboring cysteine residue, J. Biol. Chem. 273 (1998) 10835–10842.
[106] F. Sorrentino, A. Karioti, P. Gratteri, M.P. Rigobello, G. Scutari, L. Messori, A. Bindoli, M. Chioccioli, C. Gabbiani, M.C. Bergonzi, A.R. Bilia, Hypericins and thioredoxin reductase: biochemical and docking studies disclose the molecular basis for effective inhibition by naphthodianthrones, Bioorg. Med. Chem. 19 (2011) 631–641.
[107] S.-C. Sun, Non-canonical NF-κB signaling pathway, Cell Res. 21 (2011) 71–85.
[108] S. Polley, D.O. Passos, D.-B. Huang, M.C. Mulero, A. Mazumder, T. Biswas, I.M. Verma, D. Lyumkis, G. Ghosh, Structural basis for the activation of IKK1/α, Cell Rep. 17 (2016) 1907–1914.
[109] J.A. Christopher, B.G. Avitabile, P. Bamborough, A.C. Champigny, G.J. Cutler, S.L. Dyos, K.G. Grace, J.K. Kerns, J.D. Kitson, G.W. Mellor, J.V. Morey, M.A. Morse, C.F. O'Malley, C.B. Patel, N. Probst, W. Rumsey, C.A. Smith, M.J. Wilson, The discovery of 2-amino-3,5-diarylbenzamide inhibitors of IKK-α and IKK-β kinases, B *Bioorg*, Med. Chem. Lett. 17 (2007) 3972–3977.
[110] A.C. de Almeida, O.C. Marques, C. Arslanian, A. Condino-Neto, V.F. Ximenes, 4-Fluoro-2-methoxyphenol, an apocynin analog with enhanced inhibitory effect on leukocyte oxidant production and phagocytosis, Eur. J. Pharmacol. 660 (2011) 445–453.
[111] M.P.P. Kanegae, L.M. da Fonseca, I.L. Brunetti, S. de Oliveira Silva, V.F. Ximenes, The reactivity of ortho-methoxy-substituted catechol radicals with sulfhydryl groups: contribution for the comprehension of the mechanism of inhibition of NADPH oxidase by apocynin, Biochem. Pharmacol. 74 (2007) 457–464.
[112] J.L. Johnson, J.-W. Park, J.E. Benna, L.P. Faust, O. Inanami, B.M. Babior, Activation of p47 phox , a cytosolic subunit of the leukocyte NADPH oxidase: PHOSPHORYLATION OF ser-359 or ser-370 precedes phosphorylation at other sites and IS required for activity, J. Biol. Chem. 273 (1998) 35147–35152.
[113] M. Mora-Pale, M. Weïwer, J. Yu, R.J. Linhardt, J.S. Dordick, Inhibition of human vascular NADPH oxidase by apocynin derived oligophenols, Bioorg. Med. Chem. 17 (2009) 5146–5152.
[114] J. Yu, M. Weïwer, R.J. Linhardt, J.S. Dordick, The role of the methoxyphenol apocynin, a vascular NADPH oxidase inhibitor, as a chemopreventative agent in the potential treatment of cardiovascular diseases, Curr. Vasc. Pharmacol. 6 (2008) 204–217.
[115] T. Kawahara, J.D. Lambeth, Molecular evolution of Phox-related regulatory subunits for NADPH oxidase enzymes, BMC Evol. Biol. 7 (2007) 178.
[116] O. Inanami, J.L. Johnson, B.M. Babior, The leukocyte NADPH oxidase subunit p47PHOX: the role of the cysteine residues, Arch. Biochem. Biophys. 350 (1998) 36–40.
[117] J. Jiang, H. Kang, X. Song, S. Huang, S. Li, J. Xu, A model of interaction between nicotinamide adenine dinucleotide phosphate (NADPH) oxidase and apocynin analogues by docking method, Int. J. Mol. Sci. 14 (2013) 807–817.
[118] K. Kami, R. Takeya, H. Sumimoto, D. Kohda, Diverse recognition of non-PxxP peptide ligands by the SH3 domains from p67phox, Grb2 and Pex13p, EMBO J. 21 (2002) 4268–4276.
[119] A. Daina, O. Michielin, V. Zoete, SwissADME: a free web tool to evaluate pharmacokinetics, drug-likeness and medicinal chemistry friendliness of small molecules, Sci. Rep. 7 (2017) 42717.
[120] C.A. Lipinski, F. Lombardo, B.W. Dominy, P.J. Feeney, Experimental and computational approaches to estimate solubility and permeability in drug discovery and development settings, Adv. Drug Deliv. Rev. 23 (1997) 3–25.
[121] D.F. Veber, S.R. Johnson, H.-Y. Cheng, B.R. Smith, K.W. Ward, K.D. Kopple, Molecular properties that influence the oral bioavailability of drug candidates, J. Med. Chem. 45 (2002) 2615–2623.
[122] I. Muegge, S.L. Heald, D. Brittelli, Simple selection criteria for drug-like chemical matter, J. Med. Chem. 44 (2001) 1841–1846.
[123] P. Banerjee, A.O. Eckert, A.K. Schrey, R. Preissner, ProTox-II: a webserver for the prediction of toxicity of chemicals, Nucleic Acids Res. 46 (2018) W257–W263.
[124] S. Yee, In vitro permeability across caco-2 cells (colonic) can predict in vivo (small intestinal) absorption in man—fact or myth, Pharm. Res. (N. Y.) 14 (1997) 763–766.
[125] X.-l. Ma, C. Chen, J. Yang, Predictive model of blood-brain barrier penetration of organic compounds, Acta Pharmacol. Sin. 26 (2005) 500–512.
[126] S. Yamashita, T. Furubayashi, M. Kataoka, T. Sakane, H. Sezaki, H. Tokuda, Optimized conditions for prediction of intestinal drug permeability using Caco-2 cells, Eur. J. Pharmaceut. Sci. 10 (2000) 195–204.
[127] J.D. Irvine, L. Takahashi, K. Lockhart, J. Cheong, J.W. Tolan, H.E. Selick, J.R. Grove, MDCK (Madin–Darby canine kidney) cells: a tool for membrane permeability screening, J. Pharmacol. Sci. 88 (1999) 28–33.
[128] M. Yazdanian, S.L. Glynn, J.L. Wright, A. Hawi, Correlating partitioning and Caco-2 cell permeability of structurally diverse small molecular weight compounds, Pharm. Res. (N. Y.) 15 (1998) 1490.
[129] E. Li, M. Wang, Z. Wang, W. Yu, J. Chang, NBS-mediated practical cyclization of N-acyl amidines to 1,2,4-oxadiazoles via oxidative N–O bond formation, Tetrahedron 74 (2018) 4613–4618.
[130] W. Wang, H. Xu, Y. Xu, T. Ding, W. Zhang, Y. Ren, H. Chang, Base-mediated one-pot synthesis of 1,2,4-oxadiazoles from nitriles, aldehydes and hydroxylamine hydrochloride without addition of extra oxidant, Org. Biomol. Chem. 14 (2016) 9814–9822.
[131] H.A. Swarup, N. Chaithra, K. Mantelingu, K.S. Rangappa, Green synthetic approach for the construction of 3,5-disubstituted 1,2,4-oxadiazoles and

ataluren analogues from dithioesters using water, Chemistry 3 (2018) 5390–5394.
[132] B. Movassagh, F. Talebsereshki, Mild and efficient one-pot synthesis of 3,5-disubstituted 1,2,4-oxadiazoles from nitriles mediated by K_3PO_4, Synth. Commun. 44 (2014) 188–194.
[133] S. Simizu, M. Imoto, N. Masuda, M. Takada, K. Umezawa, Involvement of hydrogen peroxide production in erbstatin-induced apoptosis in human small cell lung carcinoma cells, Canc. Res. 56 (1996) 4978.